for patterning the underlying neural crest-derived ectomesenchyme [15,92]. PA epithelia could therefore constitute a possible target of RA activity resulting in distorted signalling to CNCCs.

In support of this hypothesis, it has been shown that treatment of mouse embryos with a general agonist of RA activates ectopic RA signalling in the endoderm and ectoderm lining the first two PAs. This change in epithelial patterning corresponds to a rostral shift of the expression domains of the RA-responsive genes [86].

To explore the possibility that the craniofacial lesions present in RAE could derive from altered signalling from the PA epithelium to CNCCs we performed a series of experiments on both mouse [36] and Xenopus embryos. Timed pregnant mice have been exposed to one single RA pulse at slightly different times of gestation. Craniofacial malformations of the pup only appear when RA is administered to mothers carrying embryos between 9 and 14 somites. In this temporal window CNCCs from rhombomeres 1 and 2 and the mesencephalon reach the PA1 [75]. The defects deriving from a RA treatment performed on embryos of 9 somites affected mostly proximal derivatives of the PA1 such as the proximal part of Meckel's cartilage (Mc) or the malleus, while later treatments affected both proximal and distal structures. These defects were mirrored by the progressive reduction of territories of expression of endodermal and ectodermal signals and by the downregulation of *Dlx* gene expression. Similarly, in Xenopus, RA treatment of embryos produces craniofacial defects only in a narrow temporal interval corresponding to the migration of CNCCs towards the PAs. Remarkably, in this species, RA treatments as short as one minute are sufficient to induce severe craniofacial malformations which can be observed in pre-metamorphic tadpoles several days after RA exposure of the embryos (Vieux-Rochas, unpublished observations). As RA effects are short lived due to the rapid degradation of this molecule, this experimental setting constitutes an interesting tool to study the dynamics of signalling during craniofacial morphogenesis. Our findings imply that for normal craniofacial development it is essential to protect specific signalling regions of the PA1 from the action of RA. Remarkably, the RA-degrading enzymes CYP26A1 and CYP26C1 are expressed in these regions when CNCCs reach the PA1 [93,94].

These findings reinforce the notion that the exact topography and timing of epithelial signalling to CNCC is essential to determine different craniofacial morphotypes [95]. Depending on the exact age of the embryo when RA treatment is performed, we observe the co-variance of several independent craniofacial characters resulting in morphologies that recall the primitive condition of jawed vertebrate skulls where the palatoquadrate (pq) is separated from the braincase. A particularly clear example can be seen at the level of the inner ear. The progressive transformation of the incus into a pq is paralleled by that of the malleus into the proximal part of Mc. These two simultaneous transformations generate an articulation between the proximal part of the transformed Mc and the pq, a typical character of primitive jaws, which, in modern gnathostomes, is transformed into the articulation between the malleus and the incus. Furthermore the co-variance of other characters, such as the appearance of a stylo-hyoid connection can be interpreted as an example of co-evolution of many, not functionally related, characters of the same organism. Similar mechanisms might have been

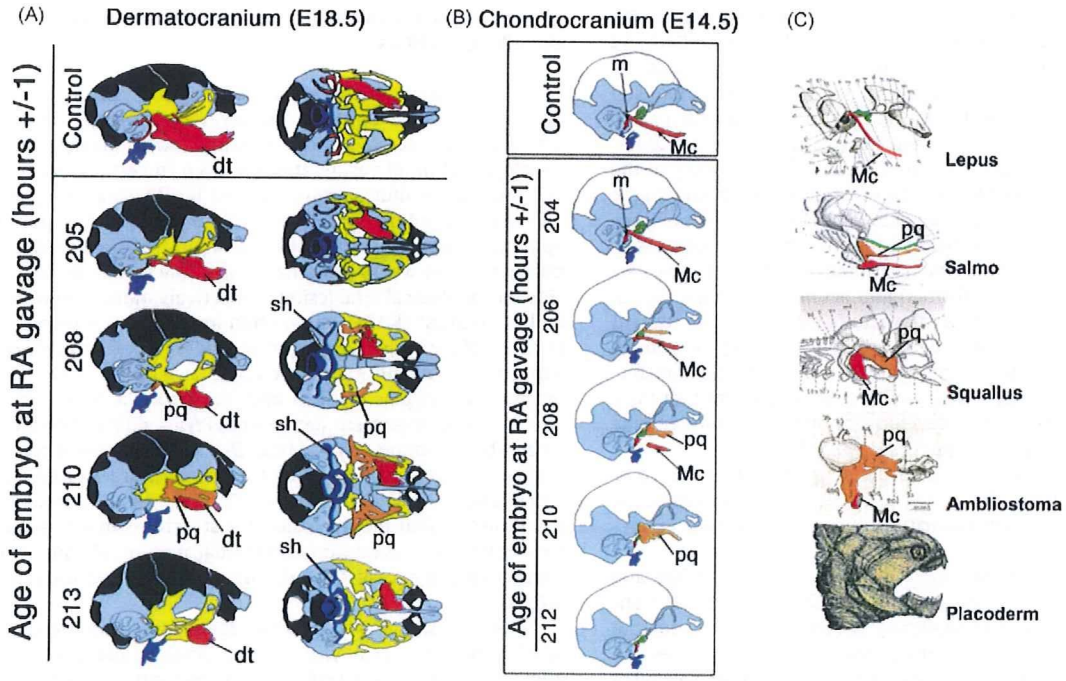

Fig. 2. Craniofacial defects induced by RA treatment.
(A) Series of drawings representing lateral and caudal views of dermatocrania of E18.5 embryos obtained after RA treatment of the mother at the indicated developmental times (expressed in hours post coitum, hpc). The main structures highlighted in colour are: the dentary (dt, red), the palatoquadrate (pq, orange), the derivatives of the maxillary component of the PA1 (yellow) and PA2 derivatives including the hyoid bone and the stylo-hyoid connection (sh, blue). Note the progressive transformation of the dentary starting at 205 hpc accompanied by the appearance of an increasingly large palatoquadrate which, in embryos treated 210 hpc, appears as two closely anastomosed parallel bars. Note also the disappearance of the tympanic ring, the opening of the palate, the deformation of the maxillary complex and of the pterygoid bone. (B) Schematic drawings representing the lateral view of chondrocrania (E14.5) of embryos which received a single RA pulse at the indicated developmental time (expressed in hpc). The main structures highlighted in colour are Meckel's cartilage (Mc, red), the neoformed palatoquadrate (pq, orange), the ala temporalis (at, green), and the hyoidean cartilage (blue). The first defect to develop is a proximal deformation of Mc with the appearance of a medially oriented cartilage bar. The malleus (m) is rapidly lost. The pq becomes progressively more prominent, to occupy most of the maxillary region of the head. (C) Hypothetical parallel between the morphologies obtained by RA treatment and the skeletal organization of different species. Abbreviations: dt, dentary; Mc, Meckel's cartilage; pq, palatoquadrate; sh, stylo-hyoid connection. Adapted from [36].

more generally involved in determining the development and evolution of animal form [36] (Fig. 2).

5. CNCC/mesoderm interactions in defining craniofacial muscle pattern

In contrast to our good understanding of how trunk skeletal muscles are formed, the signalling pathways that control head skeletal muscle morphogenesis are not yet fully elucidated.

While few craniofacial muscles, including the hypobranchial muscles and the tongue muscles develop from the first five somites, most others develop from cranial paraxial mesoderm (CPM) and lateral splanchnic mesoderm (SpM) [96,97] located in the preotic levels of the head. PA1 muscle precursors stream from the CPM and SpM into the neighbouring PA1; they then fill the PA core along with migratory CNCCs. During later PA development, crest cells surround the muscle anlagen, thereby separating the presumptive myoblasts from the overlying surface ectoderm [98–101]. Subsequently, CNCCs give rise to most skeletal elements of the head, to connective tissues and tendons [102,103]. In parallel, mesoderm-derived myoblast cells fuse together to form myofibers, which are attached to a specific CNCCs-derived skeletal element, through CNCCs-derived connective tissue. Each step of myogenesis is reflected by the expression of specific molecular markers including *Tbx1*, *Myf5*, *MyoD*, *Desmin* and *Myosin*.

The molecular mechanisms underlying head muscle patterning – myoblast guidance, positioning and connection to specific attachment sites – begin to be understood [96,104]. Furthermore, the degree to which skeletal muscle specification, differentiation and patterning is intrinsic to muscle (mesoderm) progenitors or controlled by extrinsic environmental signals (e.g. CNCCs) remains an open and fundamental question. Craniofacial shapes are amazingly diverse not only in vertebrates but also within species [e.g. dogs, birds [105,106]]. This diversity might reflect a tight link between the skeletal elements derived from the CNCCs and skeletal muscles of mesodermal origin. Indeed, it has long been suggested that in addition to contributing to the formation of skeletal elements and connective tissue in the head, CNCCs may also be involved in the patterning of the head musculature [5,74,78,98,107–113].

In a recent study [104], genetic perturbations of CNCCs development in mouse embryos and cellular perturbations of CNCCs development in avian embryos have been used to formally demonstrate that although CNCCs are not necessary for the early specification of skeletal muscle progenitors, they later play a crucial role in the migration, positioning and differentiation of cranial muscle precursors in vertebrate embryos. In the absence of CNCCs, other tissues and signals could provide some clues to promote, at least partially, skeletal muscle differentiation in the head.

Although head and trunk muscles exhibit the same tissue architecture, their development is remarkably different. The preotic head mesoderm lacks any overt sign of segmentation and never forms somites [114]. In addition, components of the molecular clock that drive trunk mesoderm segmentation and hence somite formation are only transiently expressed in cranial mesoderm [115], which soon after gastrulation merges to form a continuous strip of mesenchyme on either sides of the cranial neural tube [114].

When CPM was grafted next to axial tissues in the trunk, activation of the endogeneous myogenic program in this ectopic position was inhibited, indicating that signals from the axial tissues and surface ectoderm that stimulate myogenesis in the somite are unable to elicit this effect in CPM [116]. Consistent with the notion that myogenic activation differs between head and trunk, distinct regulatory sequences have been found to drive *Myf5* expression in these two regions of the embryo [117,118]. The concept that head and trunk muscle are generated through different regulatory pathways is also reinforced by genetic studies. While skeletal muscle formation in both regions of the embryo requires either *MyoD* or *Myf5* [119], mice lacking both *Myf5* and *Pax3* are completely devoid of trunk muscles yet retain normal head muscles [120]. In addition, mice lacking both *MyoR* and *Capsulin* display a deficit in jaw muscle formation, whereas the trunk musculature remains normal [121]. The specificity of branchiomeric muscle differentiation is also seen by the fact that certain transcription factors are involved in the control of branchiometric myogenesis but do not have an equivalent role on the rest of the axial musculature. For example, in the absence of *Tbx1*, the myogenic determination genes *Myf5* and *MyoD* fail to be normally activated in pharyngeal mesoderm [122] and branchiomeric muscle specification and differentiation are defective in *Pitx2* mutants [123].

In the head, both BMP and the canonical Wnt signalling molecules secreted by the dorsal neural tube act to repress skeletal muscle formation. This may occur via inhibition of the myogenic differentiation of the CPM in the vicinity of the neural tube. By contrast, these same Wnt ligands are required to stimulate myogenesis in the trunk. Moreover, CNCCs secrete both BMP inhibitors (Noggin, Gremlin) and Wnt inhibitors (Frzb), which together induce myogenic differentiation of the CPM in vitro [124]. Therefore, head muscle differentiation is subjected to a complex balance between neural tube-derived inhibitors and CNCCs-derived activators.

6. Human craniofacial malformations deriving from CNCCs lesions

First arch syndromes known also as oto-mandibular dysplasias or mandibulofacial dysostosis correspond to a wide spectrum of human congenital anomalies of latero-facial regions. The malformations associated with these conditions affect predominantly derivatives of the maxillary and mandibular processes of PA1. The abnormal traits display variable quantitative expression and are associated to different conditions including oculo-auriculo-vertebral spectrum (OAVS, OMIM 164210), hemifacial microsomia, Goldenhar, Franceschetti or Treacher Collins syndromes (OMIM 154500) (Fig. 3).

A possible conceptual framework to understand and classify this wide spectrum of first arch malformations is to consider that the skeletal defects result from lesions affecting the specification and differentiation of different contingents of PA1 CNCCs [125]. For example, among human first arch syndromes, we can distinguish maxillary bud pathologies (Franceschetti or Treacher Collins syndromes OMIM 154500) from mandibular bud pathologies (hemifacial microsomia or OAVS, OMIM 164210; Goldenhar syndrome). Association of maxillary and mandibular pathologies is rare and might correspond to earlier defects in CNCCs differentiation. OAVS or hemifacial microsomia is often unilateral, occurs in about 1/5600 birth [125] and displays different severity of first arch defects ranging from moderate hypoplasia to complete agenesis of the jaw with frequently associated muscle anomalies and nervous disorders.

As mentioned before, although the initial specification of CPM cells towards a myogenic program is CNCC-independent, the migration, patterning and differentiation of muscle precursors require extrinsic signals from CNCCs [104]. In line with these findings, OAVS patients present muscular defects associated to the skeletal lesion (see for example [126,127]), however, these initial descriptions where never interpreted in view of recent embryological data on the coordination of CNCCs and CPM early development. Understanding the origin of these muscular defects is very important for the prognosis of surgical intervention on OAVS patients as muscular anomalies cannot be surgically corrected as easily as skeletal malformations.

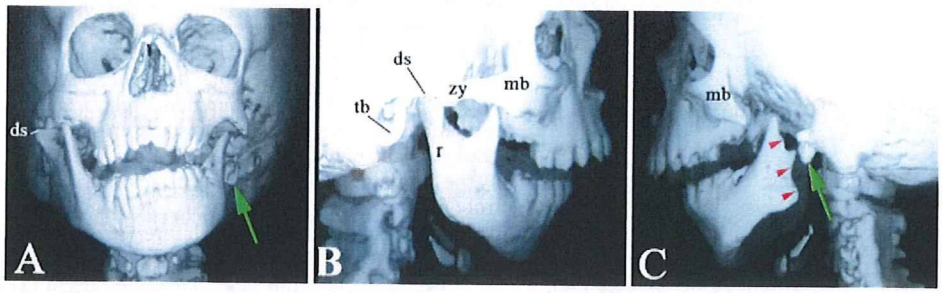

Fig. 3. Example of unilateral mandibulofacial dysostosis.
Frontal (A) and lateral (B, right; C, left) views of a three dimensional reconstruction of facial skeleton of a 6 years old child affected by left mandibulofacial dysostosis with absence of the left ramus (red arrowheads), dentary-squamosal articulation, tympanic bone and proximal zygomatic arch. An ectopic bone (green arrow) is present. The left malar bone is also hypoplastic. The medio-distal part of the mandible including lacteal and definitive teeth is unaffected. *Abbreviations*: ds, dentary-squamosal articulation; mb, malar bone; r, ramus; tb; tympanic bone; zy, zygomatic arch.

Most cases of first arch syndromes are sporadic, but familial inheritance has been reported, in particular a high load score has been found for the 14q32 genomic region which harbours the *Goosecoid* gene (*Gsc*), however, no gross mutation in the coding region was found [128] suggesting a defect in gene regulation.

7. Conclusions

Craniofacial morphogenesis is the result of complex spatio-temporal interactions between the various cellular components of the head. Molecular signals exchanged between CNCCs, mesodermal cells and endo/ectodermal epithelia of the pharyngeal arches are crucial in providing the positional information necessary to shape the different skeletal and muscular components of the head. In particular Edn1 signalling is essential to define maxilo-mandibular identity through the activation of *Dlx* genes. RA treatment of developing embryos perturbs epithelial signalling to CNCCs and has permitted to analyze their contribution to craniofacial morphogenesis. Slight changes in these signalling dynamics can result in profound changes in craniofacial morphology and might have contributed to the evolution of facial diversity. Abnormal signalling patterns could also be at the origin of congenital craniofacial malformations.

Acknowledgements

This paper was partially supported by the EU Consortium CRESCENDO (LSHM-CT-2005-018652), the ANR projects "GENDACTYL" and the "EuroRETT" consortium.

References

[1] His WS. Untersuchungen über die ertse Anlage des Wirbeltierleibes. in: Vogel FCW, editor, Die ertse Entwicklung des Hünchens im Ei. Leipzig; 1868.
[2] Platt JB. Ectodermic origin of the cartilages of the head. Anat Anz 1893;8:506–9.
[3] Platt JB. The development of the cartilaginous skull and of the branchial and hypoglossal musculature in Necturus. Morphol Jahrb 1898;25:377–464.
[4] Zottoli SJ, Seyfarth EA, Julia B. Platt (1857–1935): pioneer comparative embryologist and neuroscientist. Brain Behav Evol 1994;43(2):92–106.
[5] Noden DM. The role of the neural crest in patterning of avian cranial skeletal, connective, and muscle tissues. Dev Biol 1983;96(1):144–65.
[6] Trainor PA, Krumlauf R. Hox genes, neural crest cells and branchial arch patterning. Curr Opin Cell Biol 2001;13(6):698–705.
[7] Trainor PA. Specification and patterning of neural crest cells during craniofacial development. Brain Behav Evol 2005;66(4):266–80.
[8] Le Douarin NM. Developmental patterning deciphered in avian chimeras. Dev Growth Differ 2008;50(Suppl. 1):S11–28.
[9] Hall BK. The neural crest as a fourth germ layer and vertebrates as quadroblastic not triploblastic. Evol Dev 2000;2(1):3–5.
[10] Hall BK. The neural crest in development and evolution. New York, USA: Springer; 1999.
[11] Le Douarin N, Kalcheim H. The neural crest. Cambridge, UK: Cambridge University Press; 1999.
[12] Le Douarin NM, Creuzet S, Couly G, Dupin E. Neural crest cell plasticity and its limits. Development 2004;131(19):4637–50.
[13] Trainor PA, Sobieszczuk D, Wilkinson D, Krumlauf R. Signalling between the hindbrain and paraxial tissues dictates neural crest migration pathways. Development 2002;129(2):433–42.
[14] Couly G, Grapin-Botton A, Coltey P, Le Douarin NM. The regeneration of the cephalic neural crest, a problem revisited: the regenerating cells originate from the contralateral or from the anterior and posterior neural fold. Development 1996;122(11):3393–407.
[15] Couly G, Creuzet S, Bennaceur S, Vincent C, Le Douarin NM. Interactions between Hox-negative cephalic neural crest cells and the foregut endoderm in patterning the facial skeleton in the vertebrate head. Development 2002;129(4):1061–73.
[16] Creuzet S, Couly G, Le Douarin NM. Patterning the neural crest derivatives during development of the vertebrate head: insights from avian studies. J Anat 2005;207(5):447–59.
[17] Creuzet S, Schuler B, Couly G, Le Douarin NM. Reciprocal relationships between Fgf8 and neural crest cells in facial and forebrain development. Proc Natl Acad Sci USA 2004;101(14):4843–7.
[18] Le Douarin NM, Brito JM, Creuzet S. Role of the neural crest in face and brain development. Brain Res Rev 2007;55(2):237–47.
[19] Le Douarin NM, Dupin E. Multipotentiality of the neural crest. Curr Opin Genet Dev 2003;13(5):529–36.
[20] Le Douarin NM, Ziller C, Couly GF. Patterning of neural crest derivatives in the avian embryo: in vivo and in vitro studies. Dev Biol 1993;159(1):24–49.
[21] Creuzet S, Couly G, Vincent C, Le Douarin NM. Negative effect of Hox gene expression on the development of the neural crest-derived facial skeleton. Development 2002;129(18):4301–13.
[22] Lwigale PY, Conrad GW, Bronner-Fraser M. Graded potential of neural crest to form cornea, sensory neurons and cartilage along the rostrocaudal axis. Development 2004;131(9):1979–91.
[23] Tschopp P, Tarchini B, Spitz F, Zakany J, Duboule D. Uncoupling time and space in the collinear regulation of Hox genes. PLoS Genet 2009;5(3):e1000398.
[24] Santagati F, Rijli FM. Cranial neural crest and the building of the vertebrate head. Nat Rev Neurosci 2003;4(10):806–18.
[25] Baker CV, Bronner-Fraser M, Le Douarin NM, Teillet MA. Early- and late-migrating cranial neural crest cell populations have equivalent developmental potential in vivo. Development 1997;124(16):3077–87.
[26] Kulesa P, Ellies DL, Trainor PA. Comparative analysis of neural crest cell death, migration, and function during vertebrate embryogenesis. Dev Dyn 2004;229(1):14–29.
[27] Benouaiche L, Gitton Y, Vincent C, Couly G, Levi G. Sonic hedgehog signalling from foregut endoderm patterns the avian nasal capsule. Development 2008;135(13):2221–5.
[28] Matsushita S, Ishii Y, Scotting PJ, Kuroiwa A, Yasugi S. Pre-gut endoderm of chick embryos is regionalized by 1.5 days of development. Dev Dyn 2002;223(1):33–47.
[29] Matsushita S, Urase K, Komatsu A, Scotting PJ, Kuroiwa A, Yasugi S. Foregut endoderm is specified early in avian development through signal(s) emanating from Hensen's node or its derivatives. Mech Dev 2008;125(5–6):377–95.
[30] Withington S, Beddington R, Cooke J. Foregut endoderm is required at head process stages for anteriormost neural patterning in chick. Development 2001;128(3):309–20.
[31] Bronner-Fraser M, Sauka-Spengler T. Neural crest induction and evolution. Annu Rev Cell Dev Biol 2010 (Epub ahead of print) PMID: 19575671.
[32] Piotrowski T, Nusslein-Volhard C. The endoderm plays an important role in patterning the segmented pharyngeal region in zebrafish (*Danio rerio*). Dev Biol 2000;225(2):339–56.
[33] Brugmann SA, Tapadia MD, Helms JA. The molecular origins of species-specific facial pattern. Curr Top Dev Biol 2006;73:1–42.
[34] Nikitina N, Sauka-Spengler T, Bronner-Fraser M. Chapter 1. Gene regulatory networks in neural crest development and evolution. Curr Top Dev Biol 2009;86:1–14.

[35] Ozeki H, Kurihara Y, Tonami K, Watatani S, Kurihara H. Endothelin-1 regulates the dorsoventral branchial arch patterning in mice. Mech Dev 2004;121(4):387–95.
[36] Vieux-Rochas M, Coen L, Sato T, Kurihara Y, Gitton Y, Barbieri O, et al. Molecular dynamics of retinoic acid-induced craniofacial malformations: implications for the origin of gnathostome jaws. PLoS ONE 2007;2(6):e510.
[37] Beverdam A, Merlo GR, Paleari L, Mantero S, Genova F, Barbieri O, et al. Jaw transformation with gain of symmetry after Dlx5/Dlx6 inactivation: mirror of the past? Genesis 2002;34(4):221–7.
[38] Depew MJ, Lufkin T, Rubenstein JL. Specification of jaw subdivisions by Dlx genes. Science 2002;298(5592):381–5.
[39] Fukuhara S, Kurihara Y, Arima Y, Yamada N, Kurihara H. Temporal requirement of signaling cascade involving endothelin-1/endothelin receptor type A in branchial arch development. Mech Dev 2004;121(10):1223–33.
[40] Ruest LB, Xiang X, Lim KC, Levi G, Clouthier DE. Endothelin-A receptor-dependent and -independent signaling pathways in establishing mandibular identity. Development 2004;131(18):4413–23.
[41] Sato T, Kurihara Y, Asai R, Kawamura Y, Tonami K, Uchijima Y, et al. An endothelin-1 switch specifies maxillomandibular identity. Proc Natl Acad Sci USA 2008;105(48):18806–11.
[42] Abe M, Ruest LB, Clouthier DE. Fate of cranial neural crest cells during craniofacial development in endothelin-A receptor-deficient mice. Int J Dev Biol 2007;51(2):97–105.
[43] Clouthier DE, Hosoda K, Richardson JA, Williams SC, Yanagisawa H, Kuwaki T, et al. Cranial and cardiac neural crest defects in endothelin-A receptor-deficient mice. Development 1998;125(5):813–24.
[44] Clouthier DE, Williams SC, Yanagisawa H, Wieduwilt M, Richardson JA, Yanagisawa M. Signaling pathways crucial for craniofacial development revealed by endothelin-A receptor-deficient mice. Dev Biol 2000;217(1):10–24.
[45] Ruest LB, Kedzierski R, Yanagisawa M, Clouthier DE. Deletion of the endothelin-A receptor gene within the developing mandible. Cell Tissue Res 2005;319(3):447–53.
[46] Price M, Lemaistre M, Pischetola M, Di Lauro R, Duboule D. A mouse gene related to Distal-less shows a restricted expression in the developing forebrain. Nature 1991;351(6329):748–51.
[47] Merlo GR, Paleari L, Mantero S, Zerega B, Adamska M, Rinkwitz S, et al. The Dlx5 homeobox gene is essential for vestibular morphogenesis in the mouse embryo through a BMP4-mediated pathway. Dev Biol 2002;248(1):157–69.
[48] Panganiban G, Rubenstein JL. Developmental functions of the Distal-less/Dlx homeobox genes. Development 2002;129(19):4371–86.
[49] Merlo GR, Zerega B, Paleari L, Trombino S, Mantero S, Levi G. Multiple functions of Dlx genes. Int J Dev Biol 2000;44(6):619–26.
[50] Depew MJ, Simpson CA, Morasso M, Rubenstein JL. Reassessing the Dlx code: the genetic regulation of branchial arch skeletal pattern and development. J Anat 2005;207(5):501–61.
[51] Qiu M, Bulfone A, Ghattas I, Meneses JJ, Christensen L, Sharpe PT, et al. Role of the Dlx homeobox genes in proximodistal patterning of the branchial arches: mutations of Dlx-1, Dlx-2, and Dlx-1 and -2 alter morphogenesis of proximal skeletal and soft tissue structures derived from the first and second arches. Dev Biol 1997;185(2):165–84.
[52] Depew MJ, Simpson CA. 21st century neontology and the comparative development of the vertebrate skull. Dev Dyn 2006;235(5):1256–91.
[53] Depew MJ, Liu JK, Long JE, Presley R, Meneses JJ, Pedersen RA, et al. Dlx5 regulates regional development of the branchial arches and sensory capsules. Development 1999;126(17):3831–46.
[54] Jeong J, Li X, McEvilly RJ, Rosenfeld MG, Lufkin T, Rubenstein JL. Dlx genes pattern mammalian jaw primordium by regulating both lower jaw-specific and upper jaw-specific genetic programs. Development 2008;135(17):2905–16.
[55] Charite J, McFadden DG, Merlo G, Levi G, Clouthier DE, Yanagisawa M, et al. Role of Dlx6 in regulation of an endothelin-1-dependent, dHAND branchial arch enhancer. Genes Dev 2001;15(22):3039–49.
[56] Acampora D, Merlo GR, Paleari L, Zerega B, Postiglione MP, Mantero S, et al. Craniofacial, vestibular and bone defects in mice lacking the Distal-less-related gene Dlx5. Development 1999;126(17):3795–809.
[57] Kurihara Y, Kurihara H, Suzuki H, Kodama T, Maemura K, Nagai R, et al. Elevated blood pressure and craniofacial abnormalities in mice deficient in endothelin-1. Nature 1994;368(6473):703–10.
[58] Thomas T, Kurihara H, Yamagishi H, Kurihara Y, Yazaki Y, Olson EN, et al. A signaling cascade involving endothelin-1, dHAND and msx1 regulates development of neural-crest-derived branchial arch mesenchyme. Development 1998;125(16):3005–14.
[59] Yanagisawa H, Clouthier DE, Richardson JA, Charite J, Olson EN. Targeted deletion of a branchial arch-specific enhancer reveals a role of dHAND in craniofacial development. Development 2003;130(6):1069–78.
[60] Ruest LB, Clouthier DE. Elucidating timing and function of endothelin-A receptor signaling during craniofacial development using neural crest cell-specific gene deletion and receptor antagonism. Dev Biol 2009;328(1):94–108.
[61] Couly G, Grapin-Botton A, Coltey P, Ruhin B, Le Douarin NM. Determination of the identity of the derivatives of the cephalic neural crest: incompatibility between Hox gene expression and lower jaw development. Development 1998;125(17):3445–59.
[62] Depew MJ, Compagnucci C. Tweaking the hinge and caps: testing a model of the organization of jaws. J Exp Zool B Mol Dev Evol 2008;310(4):315–35.
[63] Yamada G, Mansouri A, Torres M, Stuart ET, Blum M, Schultz M, et al. Targeted mutation of the murine goosecoid gene results in craniofacial defects and neonatal death. Development 1995;121(9):2917–22.
[64] Bobola N, Carapuco M, Ohnemus S, Kanzler B, Leibbrandt A, Neubuser A, et al. Mesenchymal patterning by Hoxa2 requires blocking Fgf-dependent activation of Ptx1. Development 2003;130(15):3403–14.
[65] Lanctot C, Moreau A, Chamberland M, Tremblay ML, Drouin J. Hindlimb patterning and mandible development require the Ptx1 gene. Development 1999;126(9):1805–10.
[66] Byrd NA, Meyers EN. Loss of Gbx2 results in neural crest cell patterning and pharyngeal arch artery defects in the mouse embryo. Dev Biol 2005;284(1):233–45.
[67] Soprano DR, Soprano KJ. Retinoids as teratogens. Annu Rev Nutr 1995;15:111–32.
[68] Collins MD, Mao GE. Teratology of retinoids. Annu Rev Pharmacol Toxicol 1999;39:399–430.
[69] Escriva H, Holland ND, Gronemeyer H, Laudet V, Holland LZ. The retinoic acid signaling pathway regulates anterior/posterior patterning in the nerve cord and pharynx of amphioxus, a chordate lacking neural crest. Development 2002;129(12):2905–16.
[70] Lammer EJ, Chen DT, Hoar RM, Agnish ND, Benke PJ, Braun JT, et al. Retinoic acid embryopathy. N Engl J Med 1985;313(14):837–41.
[71] Mark M, Chambon P. Functions of RARs and RXRs in vivo: genetic dissection of the retinoid signaling pathway. Pure Appl Chem 2003;75(11–12):1709–32.
[72] Mallo M. Retinoic acid disturbs mouse middle ear development in a stage-dependent fashion. Dev Biol 1997;184(1):175–86.
[73] Coberly S, Lammer E, Alashari M. Retinoic acid embryopathy: case report and review of literature. Pediatr Pathol Lab Med 1996;16(5):823–36.
[74] Kontges G, Lumsden A. Rhombencephalic neural crest segmentation is preserved throughout craniofacial ontogeny. Development 1996;122(10):3229–42.
[75] Serbedzija GN, Bronner-Fraser M, Fraser SE. Vital dye analysis of cranial neural crest cell migration in the mouse embryo. Development 1992;116(2):297–307.
[76] Cheung CS, Wang L, Dong M, Chan WY. Migration of hindbrain neural crest cells in the mouse. Neuroembryology 2003;2(4):164–74.
[77] Trainor PA, Melton KR, Manzanares M. Origins and plasticity of neural crest cells and their roles in jaw and craniofacial evolution. Int J Dev Biol 2003;47(7–8):541–53.
[78] Grammatopoulos GA, Bell E, Toole L, Lumsden A, Tucker AS. Homeotic transformation of branchial arch identity after Hoxa2 overexpression. Development 2000;127(24):5355–65.
[79] Goulding EH, Pratt RM. Isotretinoin teratogenicity in mouse whole embryo culture. J Craniofac Genet Dev Biol 1986;6(2):99–112.
[80] Lee YM, Osumi-Yamashita N, Ninomiya Y, Moon CK, Eriksson U, Eto K. Retinoic acid stage-dependently alters the migration pattern and identity of hindbrain neural crest cells. Development 1995;121(3):825–37.
[81] Pratt RM, Goulding EH, Abbott BD. Retinoic acid inhibits migration of cranial neural crest cells in the cultured mouse embryo. J Craniofac Genet Dev Biol 1987;7(3):205–17.
[82] Webster WS, Johnston MC, Lammer EJ, Sulik KK. Isotretinoin embryopathy and the cranial neural crest: an in vivo and in vitro study. J Craniofac Genet Dev Biol 1986;6(3):211–22.
[83] Wei X, Makori N, Peterson PE, Hummler H, Hendrickx AG. Pathogenesis of retinoic acid-induced ear malformations in primate model. Teratology 1999;60(2):83–92.
[84] Alles AJ, Sulik KK. Pathogenesis of retinoid-induced hindbrain malformations in an experimental model. Clin Dysmorphol 1992;1(4):187–200.
[85] Sulik KK, Cook CS, Webster WS. Teratogens and craniofacial malformations: relationships to cell death. Development 1988;103(Suppl.):213–31.
[86] Matt N, Ghyselinck NB, Wendling O, Chambon P, Mark M. Retinoic acid-induced developmental defects are mediated by RARbeta/RXR heterodimers in the pharyngeal endoderm. Development 2003;130(10):2083–93.
[87] Dolle P, Ruberte E, Leroy P, Morriss-Kay G, Chambon P. Retinoic acid receptors and cellular retinoid binding proteins. I. A systematic study of their differential pattern of transcription during mouse organogenesis. Development 1990;110(4):1133–51.
[88] Iulianella A, Lohnes D. Chimeric analysis of retinoic acid receptor function during cardiac looping. Dev Biol 2002;247(1):62–75.
[89] Dupe V, Ghyselinck NB, Wendling O, Chambon P, Mark M. Key roles of retinoic acid receptors alpha and beta in the patterning of the caudal hindbrain, pharyngeal arches and otocyst in the mouse. Development 1999;126(22):5051–9.
[90] Jiang X, Choudhary B, Merki E, Chien KR, Maxson RE, Sucov HM. Normal fate and altered function of the cardiac neural crest cell lineage in retinoic acid receptor mutant embryos. Mech Dev 2002;117(1–2):115–22.
[91] Wendling O, Dennefeld C, Chambon P, Mark M. Retinoid signaling is essential for patterning the endoderm of the third and fourth pharyngeal arches. Development 2000;127(8):1553–62.
[92] Haworth KE, Healy C, Morgan P, Sharpe PT. Regionalisation of early head ectoderm is regulated by endoderm and prepatterns the orofacial epithelium. Development 2004;131(19):4797–806.
[93] Tahayato A, Dolle P, Petkovich M. Cyp26C1 encodes a novel retinoic acid-metabolizing enzyme expressed in the hindbrain, inner ear, first branchial arch and tooth buds during murine development. Gene Exp Patterns 2003;3(4):449–54.
[94] Sakai Y, Meno C, Fujii H, Nishino J, Shiratori H, Saijoh Y, et al. The retinoic acid-inactivating enzyme CYP26 is essential for establishing an uneven dis-

tribution of retinoic acid along the anterio-posterior axis within the mouse embryo. Genes Dev 2001;15(2):213–25.
[95] Shigetani Y, Sugahara F, Kawakami Y, Murakami Y, Hirano S, Kuratani S. Heterotopic shift of epithelial–mesenchymal interactions in vertebrate jaw evolution. Science 2002;296(5571):1316–9.
[96] Nathan E, Monovich A, Tirosh-Finkel L, Harrelson Z, Rousso T, Rinon A, et al. The contribution of Islet1-expressing splanchnic mesoderm cells to distinct branchiomeric muscles reveals significant heterogeneity in head muscle development. Development 2008;135(4):647–57.
[97] Harel I, Nathan E, Tirosh-Finkel L, Zigdon H, Guimaraes-Camboa N, Evans SM, et al. Distinct origins and genetic programs of head muscle satellite cells. Dev Cell 2009;16(6):822–32.
[98] Noden DM. The embryonic origins of avian cephalic and cervical muscles and associated connective tissues. Am J Anat 1983;168(3):257–76.
[99] Trainor PA, Tan SS, Tam PP. Cranial paraxial mesoderm: regionalisation of cell fate and impact on craniofacial development in mouse embryos. Development 1994;120(9):2397–408.
[100] Trainor PA, Tam PP. Cranial paraxial mesoderm and neural crest cells of the mouse embryo: co-distribution in the craniofacial mesenchyme but distinct segregation in branchial arches. Development 1995;121(8):2569–82.
[101] Hacker A, Guthrie S. A distinct developmental programme for the cranial paraxial mesoderm in the chick embryo. Development 1998;125(17):3461–72.
[102] Noden DM. Interactions and fates of avian craniofacial mesenchyme. Development 1988;103(Suppl.):121–40.
[103] Couly GF, Coltey PM, Le Douarin NM. The triple origin of skull in higher vertebrates: a study in quail-chick chimeras. Development 1993;117(2):409–29.
[104] Rinon A, Lazar S, Marshall H, Buchmann-Moller S, Neufeld A, Elhanany-Tamir H, et al. Cranial neural crest cells regulate head muscle patterning and differentiation during vertebrate embryogenesis. Development 2007;134(17):3065–75.
[105] Helms JA, Cordero D, Tapadia MD. New insights into craniofacial morphogenesis. Development 2005;132(5):851–61.
[106] Abzhanov A, Cordero DR, Sen J, Tabin CJ, Helms JA. Cross-regulatory interactions between Fgf8 and Shh in the avian frontonasal prominence. Congenit Anom (Kyoto) 2007;47(4):136–48.
[107] Couly GF, Coltey PM, Le Douarin NM. The developmental fate of the cephalic mesoderm in quail-chick chimeras. Development 1992;114(1):1–15.
[108] Ericsson R, Cerny R, Falck P, Olsson L. Role of cranial neural crest cells in visceral arch muscle positioning and morphogenesis in the Mexican axolotl, *Ambystoma mexicanum*. Dev Dyn 2004;231(2):237–47.
[109] Noden DM. Patterning of avian craniofacial muscles. Dev Biol 1986;116(2):347–56.
[110] Noden DM, Marcucio R, Borycki AG, Emerson Jr CP. Differentiation of avian craniofacial muscles: I. Patterns of early regulatory gene expression and myosin heavy chain synthesis. Dev Dyn 1999;216(2):96–112.
[111] Olsson L, Ericsson R, Cerny R. Vertebrate head development: segmentation, novelties, and homology. Theor Biosci 2005;124(2):145–63.
[112] Schilling TF, Kimmel CB. Musculoskeletal patterning in the pharyngeal segments of the zebrafish embryo. Development 1997;124(15):2945–60.
[113] Tokita M, Schneider RA. Developmental origins of species-specific muscle pattern. Dev Biol 2009;331(2):311–25.
[114] Wachtler F, Jacob M. Origin and development of the cranial skeletal muscles. Bibl Anat 1986;29:24–46.
[115] Jouve C, Iimura T, Pourquie O. Onset of the segmentation clock in the chick embryo: evidence for oscillations in the somite precursors in the primitive streak. Development 2002;129(5):1107–17.
[116] Mootoosamy RC, Dietrich S. Distinct regulatory cascades for head and trunk myogenesis. Development 2002;129(3):573–83.
[117] Hadchouel J, Tajbakhsh S, Primig M, Chang TH, Daubas P, Rocancourt D, et al. Modular long-range regulation of Myf5 reveals unexpected heterogeneity between skeletal muscles in the mouse embryo. Development 2000;127(20):4455–67.
[118] Carvajal JJ, Cox D, Summerbell D, Rigby PW. A BAC transgenic analysis of the Mrf4/Myf5 locus reveals interdigitated elements that control activation and maintenance of gene expression during muscle development. Development 2001;128(10):1857–68.
[119] Rudnicki MA, Schnegelsberg PN, Stead RH, Braun T, Arnold HH, Jaenisch R. MyoD or Myf-5 is required for the formation of skeletal muscle. Cell 1993;75(7):1351–9.
[120] Tajbakhsh S, Rocancourt D, Cossu G, Buckingham M. Redefining the genetic hierarchies controlling skeletal myogenesis: Pax-3 and Myf-5 act upstream of MyoD. Cell 1997;89(1):127–38.
[121] Abu-Issa R, Smyth G, Smoak I, Yamamura K, Meyers EN. Fgf8 is required for pharyngeal arch and cardiovascular development in the mouse. Development 2002;129(19):4613–25.
[122] Kelly RG, Jerome-Majewska LA, Papaioannou VE. The del22q11.2 candidate gene Tbx1 regulates branchiomeric myogenesis. Hum Mol Genet 2004;13(22):2829–40.
[123] Dong F, Sun X, Liu W, Ai D, Klysik E, Lu MF, et al. Pitx2 promotes development of splanchnic mesoderm-derived branchiomeric muscle. Development 2006;133(24):4891–9.
[124] Tzahor E, Kempf H, Mootoosamy RC, Poon AC, Abzhanov A, Tabin CJ, et al. Antagonists of Wnt and BMP signaling promote the formation of vertebrate head muscle. Genes Dev 2003;17(24):3087–99.
[125] Gorlin RJ. In: Gorlin RJ, Cohen MM, Hennekam RCM, editors. Branchial arch and oro-acral disorders. London: Oxford Univ. Press; 2001. p. 641–9.
[126] Marsh JL, Baca D, Vannier MW. Facial musculoskeletal asymmetry in hemifacial microsomia. Cleft Palate J 1989;26(4):292–302.
[127] Hirschfelder U, Piechot E, Schulte M, Leher A. Abnormalities of the TMJ and the musculature in the oculo-auriculo-vertebral spectrum (OAV). A CT study. J Orofac Orthop 2004;65(3):204–16.
[128] Kelberman D, Tyson J, Chandler DC, McInerney AM, Slee J, Albert D, et al. Hemifacial microsomia: progress in understanding the genetic basis of a complex malformation syndrome. Hum Genet 2001;109(6):638–45.

Neuropharmacology 58 (2010) 774–783

Contents lists available at ScienceDirect

Neuropharmacology

journal homepage: www.elsevier.com/locate/neuropharm

Cilostazol improves cognitive function in mice by increasing the production of insulin-like growth factor-I in the hippocampus

Juan Zhao [a], Naoaki Harada [a], Hiroki Kurihara [b], Naomi Nakagata [c], Kenji Okajima [a,*]

[a] Departments of Translational Medical Science Research, Nagoya City University Graduate School of Medical Sciences, Kawasumi 1, Mizuho-cho, Mizuho-ku, Nagoya 467-8601, Japan
[b] Department of Physiological Chemistry and Metabolism, University of Tokyo, Graduate School of Medicine, Tokyo, Japan
[c] Division of Reproductive Engineering, Center for Animal Resources and Development, Kumamoto University, Kumamoto, Japan

ARTICLE INFO

Article history:
Received 1 May 2009
Received in revised form
19 November 2009
Accepted 13 December 2009

Keywords:
Cilostazol
Insulin-like growth factor-I
Cognitive function
Sensory neuron
Hippocampus

ABSTRACT

Insulin-like growth factor I (IGF-I) exerts beneficial effects on cognitive function by inducing angiogenesis and neurogenesis in the hippocampus. We demonstrated that stimulation of sensory neurons in the gastrointestinal tract increased IGF-I production in the hippocampus, and thereby improved cognitive function in mice. Since cAMP plays a critical role in stimulation of sensory neurons, the type III phosphodiesterase (PDE3) inhibitor cilostazol might increase IGF-I production in the hippocampus by stimulating sensory neurons and thus improve cognitive function in mice. We tested this hypothesis in the present study. Cilostazol increased the release of calcitonin gene-related peptide (CGRP) and levels of cAMP in dorsal root ganglion (DRG) neurons isolated from wild-type (WT) mice. Tissue levels of cAMP in the DRG and hippocampus and those of CGRP, IGF-I, and IGF-I mRNA in the hippocampus were increased after 4-week oral administration of cilostazol to WT mice. Levels of expression of *c-fos* in the spinal dorsal horns, parabrachial nuclei, the solitary tract nucleus, and the hippocampus were also increased in these animals. Significant enhancement of angiogenesis and neurogenesis was observed in the dentate gyrus of the hippocampus after cilostazol administration in WT mice. Significant improvement of spatial learning was also observed in WT mice administered cilostazol. However, none of these effects in WT mice were observed in CGRP-knockout mice. These observations suggest that cilostazol may improve cognitive function in mice by increasing the hippocampal production of IGF-I through stimulation of sensory neurons.

1. Introduction

Cilostazol, 6-[4-(1-cyclohexyl-1*H*-tetrazol-5-yl)butoxy]-3,4-dihydro-2- (1*H*)-quinolinone, a potent inhibitor of type III phosphodiesterase (PDE3), has been shown to increase cellular levels of cAMP by inhibiting degradation of it, and to thereby inhibit platelet aggregation (Kimura et al., 1985). It has been approved as a therapeutic agent for intermittent claudication by the Food and Drug Administration (Dawson et al., 1998). Recently, cilostazol was shown to prevent cerebral ischemic infarction via an anti-apoptotic neuroprotective effect in rats (Choi et al., 2002). Cilostazol has also been found to protect against brain white matter damage and cognitive impairment in a rat model of chronic cerebral hypoperfusion (Watanabe et al., 2006). However, the mechanisms underlying these neuroprotective effects of cilostazol are not fully understood.

Insulin-like growth factor-I (IGF-I) is a basic peptide composed of 70 amino acids, and is with ubiquitously distributed in various tissues and cells (Daughaday and Rotwein, 1989). It mediates the growth-promoting effects of growth hormone (GH) and plays important roles in postnatal and adolescent growth (Daughaday and Rotwein, 1989). IGF-I has been shown to have neuroprotective effects, and to improve the neurological function in animals subjected to ischemic brain injury (Guan, 2008). IGF-I has also been shown to enhance excitatory synaptic transmission in the CA_1 region of the hippocampus (Ramsey et al., 2005) and to improve spatial learning by inducing neurogenesis in the hippocampus (Aberg et al., 2000). The impairment of spatial learning in mice caused by low serum levels of IGF-I can be reversed by exogenous administration of IGF-I (Trejo et al., 2008). A close correlation has been found between plasma IGF-I level and cognitive function in

Abbreviations: BrdU, 5-bromo-2′-deoxyuridine; CGRP, calcitonin gene-related peptide; DG, dentate gyrus; DRG, dorsal root ganglion; GFAP, glial fibrillary acidic protein; GH, growth hormone; IGF-I, insulin-like growth factor-I; NTS, solitary tract nucleus; PBN, parabrachial nuclei; PBS, phosphate-buffered saline; PKA, protein kinase A; TRPV1, transient receptor potential vanilloid 1; VEGF, vascular endothelial growth factor; WT, wild-type; SGZ, subgranular zone; GCL, granule cell layer.

* Corresponding author. Tel.: +81 52 853 8196; fax: +81 52 842 3460.
E-mail address: whynot@med.nagoya-cu.ac.jp (K. Okajima).

0028-3908/$ – see front matter © 2009 Elsevier Ltd. All rights reserved.
doi:10.1016/j.neuropharm.2009.12.008

older individuals (Landi et al., 2007). These observations strongly suggest that IGF-I may improve cognitive function by increasing plasticity and promoting neurogenesis in the hippocampus.

Capsaicin-sensitive sensory neurons are nociceptive neurons that are found in many tissues: within the lining epithelia, around blood vessels, and in the nonvascular smooth muscle and myocardium of the atria (Maggi and Meli, 1988). These sensory neurons release calcitonin gene-related peptide (CGRP) following stimulation by a wide variety of noxious physical and chemical agents through activation of the transient receptor potential vanilloid 1 (TRPV1) expressed on them (Dray, 1995), and thereby exert sensory-efferent functions. CGRP, a 37-amino acid neuropeptide, is produced by alternative splicing of the calcitonin gene (Rosenfeld et al., 1992). It is widely distributed in the central and peripheral nervous systems (Dobolyi et al., 2005) and has diverse functions (van Rossum et al., 1997). We previously reported that CGRP rapidly increases IGF-I production by increasing transcription of the IGF-I gene in various tissues including the brain of mice administered capsaicin (Harada et al., 2007). Capsaicin-sensitive sensory neurons containing CGRP are also present in the gastrointestinal tract, and are predominantly spinal in origin (Ward et al., 2003). Furthermore, nociceptive information from the gastrointestinal tract is transmitted to the hippocampus via the spino-parabrachial pathway (Gauriau and Bernard, 2002). Consistent with these observations, we previously found that stimulation of sensory neurons in the gastrointestinal tract increases IGF-I production in the hippocampus via activation of the spino-parabrachial pathway in mice (Narimatsu et al., 2009).

Since protein kinase A (PKA) activation has been shown to induce phosphorylation of TRPV1, which sensitizes sensory neurons to activation by endogenous agonists (Tominaga et al., 2001), it is possible that the PDE3 inhibitor cilostazol is capable of stimulating sensory neurons in the gastrointestinal tract by increasing cellular cAMP levels and thereby promoting IGF-I production in the hippocampus. Cilostazol might thus improve cognitive function. To test whether this is the case in the present study, we examined the effect of oral administration of cilostazol on hippocampal IGF-I production and cognitive function in wild-type (WT) and CGRP-knockout (CGRP−/−) mice.

2. Materials and methods

2.1. Animals

All procedures were conducted in accordance with the National Institute of Heath guidelines for the Care and Use of Laboratory Animals and protocols approved by the Nagoya City University Animal Care Committee. CGRP−/− and their C57BL/6 wild-type (WT) (Nihon SLC, Hamamatsu, Japan) littermates were used. All animals were males aged 6–10 weeks, weight between 18 and 24 g. Mice were given free access to food and water throughout the experiment.

2.2. Generation of αCGRP-knockout mice

The generation of αCGRP-knockout mice was described previously (Oh-hashi et al., 2001). The mouse CT/αCGRP genomic DNA was cloned from a BALB/c mouse genomic library in EMBL3 using synthetic oligonucleotide probes derived from the mouse CT/αCGRP cDNA sequence. A 7.0-kb fragment containing exons 3–5 of the mouse CT/αCGRP gene was subcloned into pBluescript (Stratagene). A targeting vector was constructed by replacing the 1.6-kb XbaI–XbaI fragment encompassing exon 5, which is specific for αCGRP, with the neomycin resistance gene and flanking the thymidine kinase gene. This plasmid was linearized with NotI and introduced into 129/Sv-derived SM-1 ES cells by electroporation, after which the cells were selected in medium containing G418 (300 μg/mL) and ganciclovir (2 μmol/L). Homologous recombinants were identified by PCR and Southern blot analysis. Targeted ES cell clones were injected into C57BL/6 mouse blastocysts to generate chimeric mice. Male chimeras were then crossbred with C57BL/6 females and germline transmission was achieved. Littermates obtained by breeding heterozygotes with the genetic background of the 129/SvC57BL/6 hybrid were used for phenotypic analysis. Only males were used in this study.

2.3. Genotype determination of CGRP-knockout pups

Genomic DNA was extracted from tails of mice as previously described (Oh-hashi et al., 2001), and was used for PCR analysis. PCR was performed using the external primers of the replaced gene fragment. The wild-type allele and the mutant allele gave different band sizes. Primer sequences and PCR conditions have been described (Harada et al., 2006; Oh-hashi et al., 2001).

2.4. Regents and administration

Cilostazol (OPC-13013) [6-[4-(1-cyclohexyl-1*H*-tetrazol-5-yl) butoxy]-3,4-dihydro-2-(1*H*)-quinolinone], was generously donated by Otsuka Pharmaceutical co. Ltd. (Tokushima, Japan). Mice of the cilostazol administration group were provided laboratory food containing cilostazol at 10, 30, and 160 mg/kg per day for 4 weeks. After the behavioral testing, mice were killed under anesthesia with i.p. injection of ketamine (100 mg/kg) and xylazine (10 mg/kg). The hippocampus of mice was removed for determination of CGRP and IGF-I levels. For immunohistochemistry sample, mice were intraperitoneally injected with 5-bromo-2′-deoxyuridine (BrdU) (50 mg/kg; Sigma Chemical Co.) for 5 consecutive days before euthanization. All other reagents were of analytical grade.

2.5. Isolation and culture of dorsal root ganglion (DRG) neurons

The lumbar, cervical, and thoracic DRGs were dissected from both sides of spinal cord of mice as previously described (Harada et al., 2006). After 5 days in culture, the medium was aspirated gently and washed with serum-free Ham's F-12 medium. Cells were incubated with cilostazol (1, 10 μM) or vehicle for 30 min in Ham's F-12 medium containing 1% supplemented calf serum without nerve growth factor. After incubation, the supernatants were collected and stored at −20 °C for CGRP measurement. Thereafter, ice-cold 65% ethanol was added to each well and incubated on-ice for 20 min. Finally, ethanol was collected for determination of intracellular cAMP levels with an enzyme immunoassay kit (GE Healthcare, Buckinghamshire, UK) according to the manufacture's instructions. CGRP levels were determined as described below.

2.6. Morris water maze task

Behavioral testing was conducted as described previously (Ryan et al., 2008). We used a circular pool (150 cm diameter). The pool was filled with water at 30 °C and contained a round-shaped transparent acrylic platform (10 cm diameter). In the task, the platform was submerged 1 cm below the surface of the water and located in the southeast quadrant of the pool throughout the trials. After a mouse was put into the pool, each had a maximum of 90 s to locate and climb onto the platform (one trial). When a mouse located the platform, it was allowed to stay on it for 20 s. Mouse that did not find the platform in the allowed time was placed on it by the experimenter and left there for 20 s. Animals were trained in the Morris water maze for one trial per day for 5 days. Reference memory test (probe trial) was performed in the absence of the platform 2 h after the last trial. During the reference memory test, the trial was performed with the cutoff time of 90 s. The latency to reach the platform, swim speed and, for the reference memory tests, time spent in the target area (zone radius: 30 cm, three times the target diameter) were recorded with a digital camera system,

2.7. Determination of CGRP level

Tissue levels of CGRP were determined in mice by a modification of the methods described previously (Harada et al., 2006). Hippocampus were weighted and homogenized in 0.5 ml of 2 N acetic acid. Homogenates were bathed in 90 °C water for 20 min and then centrifuged at 4500 g for 10 min (4 °C). CGRP was extracted from the supernatant using reverse-phage C18 columns (Amersham, Little Chalfont, UK). Columns were prepared by washing with 5 ml methanol onto the colum followed by a wash with 20 ml of 0.1% trifluoroacetic acid, and the solvent was evaporated under a stream of nitrogen gas. The concentration of CGRP was assayed by using a specific enzyme immunoassay kit (SPI-BIO, Massy, France). The sensitively of the CGRP assay was 10 pg/ml. The antiserum cross-reacted 100% of rodent α- and β-CGRP according to the manufacturer's data sheet. Results are expressed as micrograms of CGRP per gram of tissue.

2.8. Determination of hippocampal IGF-I level

Hippocampal tissue levels of IGF-I were determined in animals by modification of the methods as described previously (Harada et al., 2007). The hippocampus was minced and homogenized in 0.5 mL of 1 N acetic acid according to the manufacturer's instruction. The homogenates were then centrifuged at 3000 g for 10 min. The supernatants were kept at −80 °C until assayed for IGF-I concentration by using a specific enzyme immunoassay kit (Diagnostic Systems Laboratories Inc., Webster, TX). In this ELISA method, samples were incubated with a regent that is capable of dissociating IGF-I from binding proteins.

2.9. Quantitative mRNA analysis

Quantitative mRNA analysis was performed as described previously (Harada et al., 2007). Total RNA of hippocampus was extracted from the hippocampus with TRIzol reagent (Invitrogen) according to the manufacturer's instruction. RNA extracted was used as a template for cDNA reverse transcription. Sample cDNAs were amplified in the model 7700 Sequence detector (Applied Biosystems, Foster City, CA) with primers, dual-labeled fluogenic probes, and a Taqman PCR Reagent Kit (Applied Biosystems). Thermal cycler conditions were 10 min at 95 °C for deactivation preceding 40 cycles for 15 s at 95 °C for denaturation and 1 min at 60 °C for bath annealing and extension. Known concentrations of serially diluted IGF-I and β-actiin cDNA generated by PCR were used as standards for quantity of sample cDNA. Copy numbers of cDNA for IGF-I were standardized by those for β-actiin from same sample.

3. Measurement of cAMP

Frozen Hippocampal tissues were weighed and then homogenized in 1 ml 5% (wt/vol) trichloroacetic acid. Isolated DRG neurons were homogenized in 0.5 ml 5% (wt/vol) trichloroacetic acid. After centrifugation to remove precipitated protein, the trichloroacetic acid was extracted three times with 5 ml of water-saturated diethyl ether. The solvent was evaporated under a stream of nitrogen gas at 60 °C. The concentration of cAMP was measured in duplicate determinations by using an EIA kit purchased from GE Healthcare. DRG neurons protein was measured by a modified Bradford assay with bovine serum albumin as the standard.

3.1. Immunohistochemistry

For histochemical analysis, mice were anesthetized and perfused with 0.01 M phosphate-buffered saline (PBS) followed by 4% paraformaldehyde in PBS. Brains were removed and post-fixed for 24 h in 4% paraformaldehyde in 0.1 M PBS (pH 7.4), and then stored in PBS with 20% sucrose for 24 h. The isolated brains were frozen in an OCT compound (Tissue Tec; Miles, Elkhart, IN, USA) and serial sections at 20 μM thickness were used for immunofluorescence as described (Eriksson et al., 1998). Samples for BrdU staining were treated for DNA denaturation with 2 N HCl. Sections were incubated with primary antibodies at the following concentrations: rabbit anti-c-fos polyclonal antibody (1:500; Santa Cruz Biotechnology Inc., Santa Cruz, CA), mouse anti-IGF-I monoclonal antibody (1:200; Upstate Biotechnology), rabbit anti-glial fibrillary acidic protein (GFAP) polyclonal antibody (1:1000; Dako, Glostrup, Denmark), mouse anti-BrdU monoclonal antibody (1:100; Invitrogen), rat anti-BrdU monoclonal antibody (1:400; Abcam), rat anti-CD31 monoclonal antibody (1:200; BD Biosciences PharMingen, San Diego, CA), and mouse anti-calbindin-D28k monoclonal antibody (1:200; Abcam, Cambridge, UK). After incubating at 4 °C overnight and washing, the sections were treated with secondary antibodies, Alexa Fluor 568 anti-rabbit IgG for c-fos, Alexa Fluor 488 anti-mouse IgG for IGF-I, BrdU(anti-mouse) and calbindin-D28k, Alexa Fluor 568 anti-rabbit IgG for GFAP, Alexa Fluor 594 anti-rat IgG for BrdU (anti-rat), and Alexa Fluor 594 anti-rat IgG for CD31 (1:500; Invitrogen) for 1 h at room temperature. Negative controls were performed by omitting the primary antibodies during the immunostaining. Samples were then mounted and photographed under light Fluorescence microscope (Axio Image A1, Carl Zeiss).

3.2. Quantification and statistical analysis

The BrdU-positive cells in the subgranular (SGZ), granule cell layer (GCL) and in the hilus of the hippocampus was counted using the stereological counting method. Five sections from the hippocampus were cut beginning 1.46 mm caudal and 1.86 mm anterior to the bregma with intervals of 100 μm. To assess the phenotype of BrdU-positive cell in double-immunofluorescence, a mean value for each marker was obtained from 5 sections from 5 mice. The number of *c-fos* labeled cells was quantified in the dorsal horn (lamina I–II) of spinal cord, parabrachial nuclei (PBN), the solitary tract nucleus (NTS), and the hilus of the hippocampus. The number of cells from NTS, PBN and hilus was counted from three sections of each brain ($n = 5$ for each group), corresponding to planes 6.64, 4.96 and 1.86 mm anterior to bregma. Due to the spread localization of GFAP, we used fluorescence intensity to quantify the average intensity of each field by Image J software, and the data were expressed as % intensity.

Data are expressed as the mean ± SEM. The results were compared using an ANOVA followed by Dunnett's multiple comparison test or the unpaired student's *t*-test was used for the data came from two groups. A level of $p < 0.05$ was considered statistically significant.

4. Results

4.1. Effect of cilostazol on CGRP release and cellular cAMP levels in cultured DRG neurons isolated from WT mice

To determine whether cilostazol stimulates sensory neurons by increasing cellular cAMP levels, we examined the effects of cilostazol on the release of CGRP and cellular cAMP levels in cultured DRG neurons isolated from WT mice. Cilostazol significantly increased the release of CGRP from cultured DRG neurons isolated from WT mice in a concentration-dependent fashion ($F_{2, 12} = 110.4$, $p < 0.01$) (Fig. 1A). It also increased cellular cAMP levels in cultured DRG neurons ($F_{2, 12} = 68.88$, $p < 0.01$) (Fig. 1B).

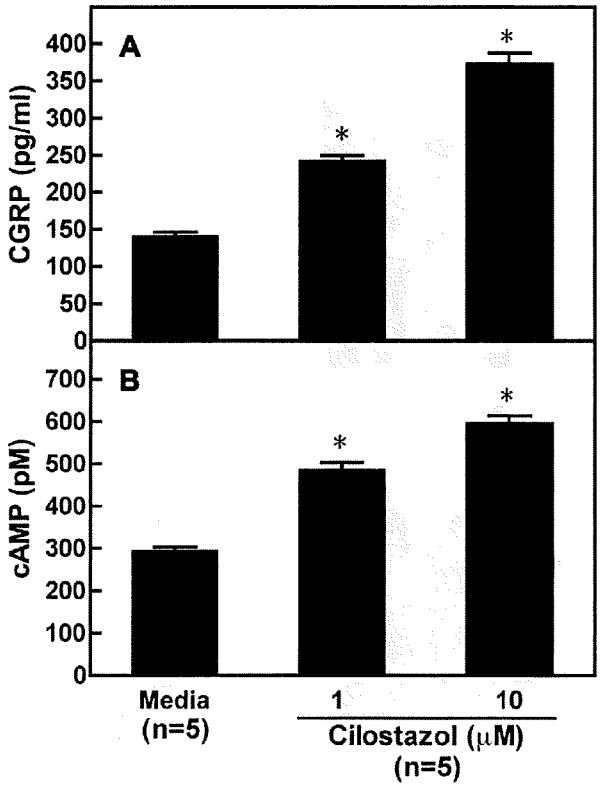

Fig. 1. Effect of cilostazol on CGRP release (A) and intracellular cAMP levels (B) in cultured dorsal root ganglion (DRG) neurons isolated from WT mice. DRG neurons were incubated with cilostazol (1–10 μM) for 30 min. Supernatants were collected and CGRP levels were measured by enzyme immunoassay. Intracellular cAMP levels were measured by enzyme immunoassay. Values are expressed as means ± S.E.M. from five experiments. *, $p < 0.01$ vs. media; one-way ANOVA.

4.2. Effect of cilostazol on tissue levels of cAMP in the DRG and hippocampus of WT and CGRP−/− mice

Tissue levels of cAMP in the DRG and hippocampus were measured in WT and CGRP−/− mice after oral administration of cilostazol for 4 weeks. Baseline tissue levels of cAMP in the DRG ($F_{1,\ 16} = 276.37$, $p < 0.01$) were significantly lower in CGRP−/− mice than in WT mice (Fig. 2A). Administration of cilostazol at 30 and 160 mg/kg/day significantly increased cAMP levels in the DRG of WT mice ($F_{3,\ 16} = 12.49$, $p < 0.01$), but not in the DRG of CGRP−/− mice (Fig. 2A). Tissue levels of cAMP in the hippocampus after administration of cilostazol at 160 mg/kg/day were significantly increased in WT mice ($F_{3,\ 16} = 3.360$, $p < 0.05$) but not in CGRP−/− mice (Fig. 2B).

4.3. Effect of cilostazol on tissue levels of CRGP, IGF-I, and IGF-I mRNA in the hippocampus of WT and CGRP−/− mice

To determine whether cilostazol increases tissue levels of CGRP, IGF-I, and IGF-I mRNA in the hippocampus of mice by stimulating sensory neurons, we determined the tissue levels of these substances in the hippocampus of WT and CGRP−/− mice following cilostazol administration for 4 weeks. Baseline tissue levels of CGRP ($F_{1,\ 16} = 680.83$, $p < 0.01$), IGF-I ($F_{1,\ 16} = 196.73$, $p < 0.01$), and IGF-I mRNA ($F_{1,\ 16} = 559.18$, $p < 0.01$) were significantly lower in CGRP−/− mice than in WT mice (Fig. 3). Oral administration of cilostazol at 30 and 160 mg/kg/day significantly

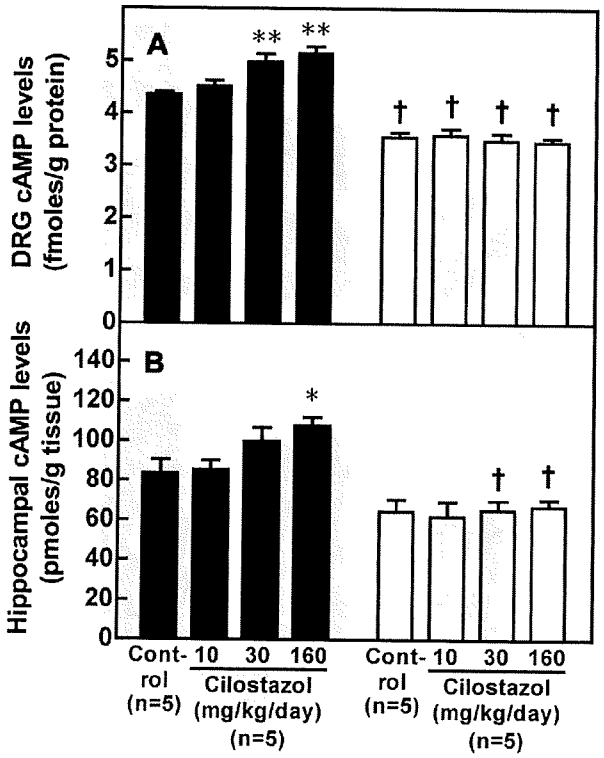

Fig. 2. Effect of cilostazol on tissue levels of cAMP in DRG (A) and hippocampus (B) in WT and CGRP−/− mice. DRG and hippocampus were removed at 4 weeks after oral administration of cilostazol. Levels of cAMP were measured in the DRG (A) and the hippocampus (B) in WT (solid bars) and CGRP−/− mice (open bars). Data are expressed as mean ± S.E.M. from five experiments. *, $p < 0.05$ vs. control; **, $p < 0.01$ vs. control, one-way ANOVA; †, $p < 0.01$ vs. WT mice, two-way ANOVA.

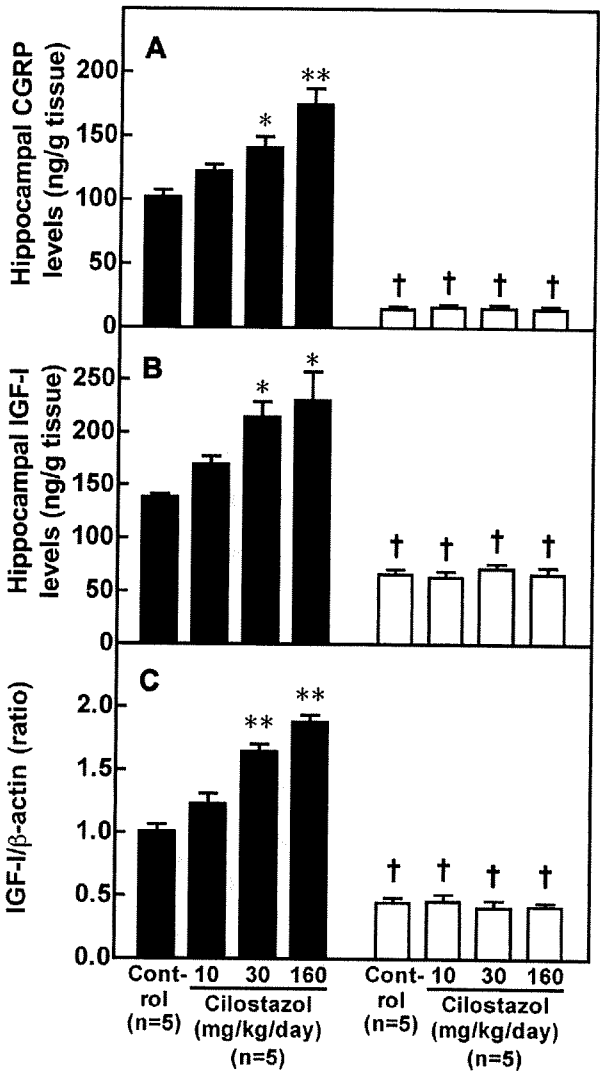

Fig. 3. Effect of cilostazol on hippocampal levels of CGRP (A) and IGF-I (B) in WT and CGRP−/− mice. Hippocampus was removed at 4 weeks after oral administration of cilostazol. Values are means ± S.E.M. from five animal experiments. Solid bars, WT mice; open bars, CGRP−/− mice. *, $p < 0.05$ vs. control, **, $p < 0.01$ vs. control, one-way ANOVA; †, $p < 0.01$ vs. WT mice, two-way ANOVA.

increased tissue levels of CGRP ($F_{3,\ 12} = 11.73$, 30 mg/kg/day: $p < 0.05$; 160 mg/kg/day: $p < 0.01$), IGF-I ($F_{3,\ 12} = 5.542$, $p < 0.05$), and IGF-I mRNA ($F_{3,\ 12} = 34.29$, $p < 0.01$) in the hippocampus of WT, but not CGRP−/− mice (Fig. 3). In neither WT nor CGRP−/− mice were serum IGF-I levels increased after administration of cilostazol at these dosages (data not shown).

4.4. Effect of cilostazol on immunohistochemical expression of IGF-I in the hippocampus of WT mice

Expression of IGF-I in the hippocampus of WT mice was examined by immunofluorescence staining. Double-immunofluorescence staining for IGF-I (Fig. 4, a and d) and GFAP (Fig. 4, b and e) showed that IGF-I immunoreactivity was co-localized with immunoreactivity for astrocytes in WT mice (Fig. 4, c and f). Increase in the number of IGF-I immunoreactivity co-localized with

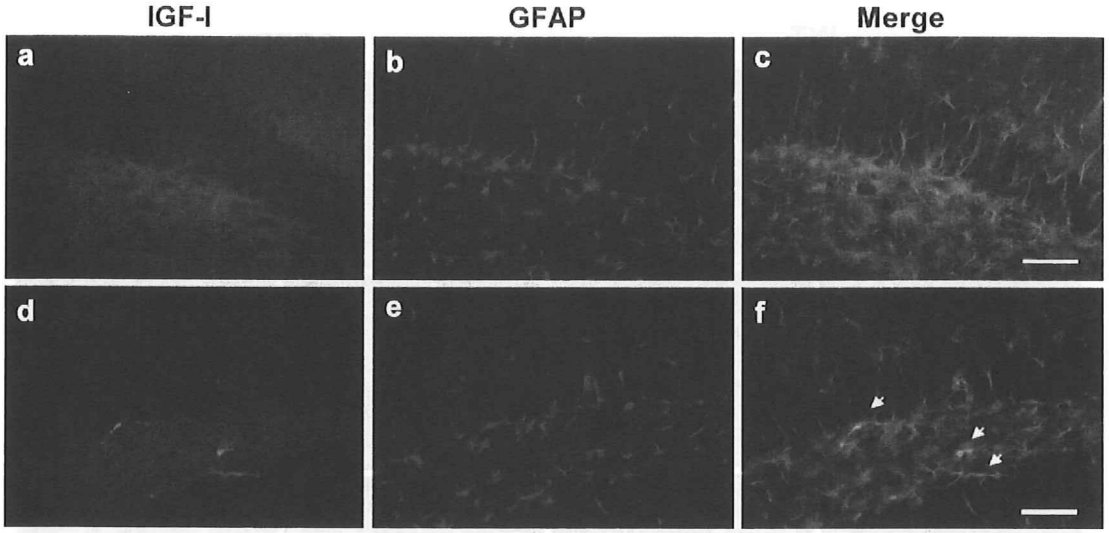

Fig. 4. Effect of cilostazol administration on immunohistochemical expression of IGF-I in the hippocampus of WT mice. Immunohistochemical expression of IGF-I in dentate gyrus (DG) of WT mice was increased by cilostazol treatment (d) compared with control (a). Double-immunofluorescence staining of IGF-I (a, d) and GFAP (b, e) for detection of astrocytes showed that IGF-I positive cell could specifically co-express GFAP (arrows in f). Scale bars = 50 μm.

GFAP immunoreactivity was observed in the SGZ and hilus of the DG after 4-week oral administration of cilastazol at 160 mg/kg/day ($p < 0.01$) (Fig. 5). The intensity of GFAP immunoreactivity was not significantly affected by administration of cilostazol (data not shown).

4.5. *Effect of cilostazol on c-fos expression in the spinal and brain nuclei in WT and CGRP−/− mice*

Induction of *c-fos* expression is a well established marker of neuronal activation, and immunohistological detection of *c-fos* allows mapping of activated brain nuclei, and thus mapping of functional pathways (Sagar et al., 1988). To examine the mechanisms involved and pathway of the relay system that leads to increase in hippocampal IGF-I production in WT mice after oral administration of cilostazol at 160 mg/kg/day, we determined *c-fos* expression in the spinal and supraspinal nervous tissues of WT and CGRP−/− mice administered cilostazol. The location and approximate size of the area of analysis for each region was adapted from an atlas of the mouse spinal cord and a mouse brain atlas as reported previously (Narimatsu et al., 2009). In WT mice, cilostazol-induced changes in neuronal activity were observed in the dorsal horn (lamina I–II) of the spinal cord and the nucleus of the solitary tract (NTS), parabrachial nuclei (PBN), and hippocampus, as determined by increased density of cellular *c-fos* expression (Figs. 6 and 7). In contrast, no such increases in *c-fos* expression were observed in CGRP−/− mice after oral administration of cilostazol (Figs. 6 and 7).

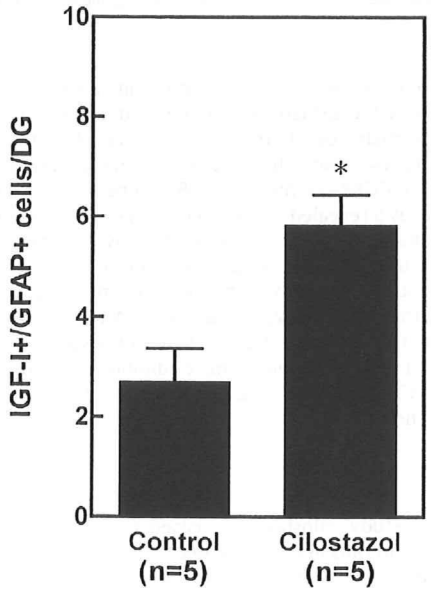

Fig. 5. Effect of cilostazol on the number of cells showing co-localization of IGF-I- and GFAP in the hippocampus of WT mice. Values are expressed as means ± S.E.M. from five experiments. *, $p < 0.01$ vs. control, unpaired student's *t*-test.

4.6. *Effect of cilostazol on the hippocampal angiogenesis and neurogenesis in WT and CGRP−/− mice*

To determine the effect of cilostazol on neurogenesis in the hippocampus of the mouse, co-localization of BrdU immunoreactivity with immunoreactivity for the granule cell marker Calbindin D28k, the astrocyte marker GFAP, and the endothelial marker CD31 was investigated. After 4-week administration of cilostazol at 160 mg/kg/day the majority of surviving new cells (BrdU + cells) had differentiated into mature neurons (BrdU+/calbindin-D28 + cells) and endothelial cells (BrdU+/CD31 + cells) in SGZ of the DG in WT mice (Fig. 8). A much smaller proportion of BrdU + cells were also identified as astrocytes (BrdU+/GFAP + cells) (Fig. 8).

The number of BrdU + cells in DG was significantly lower in CGRP−/− mice than in WT mice ($F_{1,16} = 180.16$, $p < 0.01$) (Fig. 8A). Further significant increase in the number of BrdU + cells in DG was observed in WT mice after oral administration of cilostazol at 160 mg/kg/day for 4 weeks ($F_{3,16} = 15.74$, $p < 0.01$), while no such increase was found in the CGRP−/− mice (Fig. 7A).

Numbers of BrdU+/CD31+ ($F_{3,16} = 290.23$, $p < 0.01$), BrdU+/calbindin-D28k+ ($F_{1,16} = 214.76$, $p < 0.01$), and BrdU+/GFAP+ ($F_{1,16} = 134.31$, $p < 0.01$) cells in the DG were significantly lower in

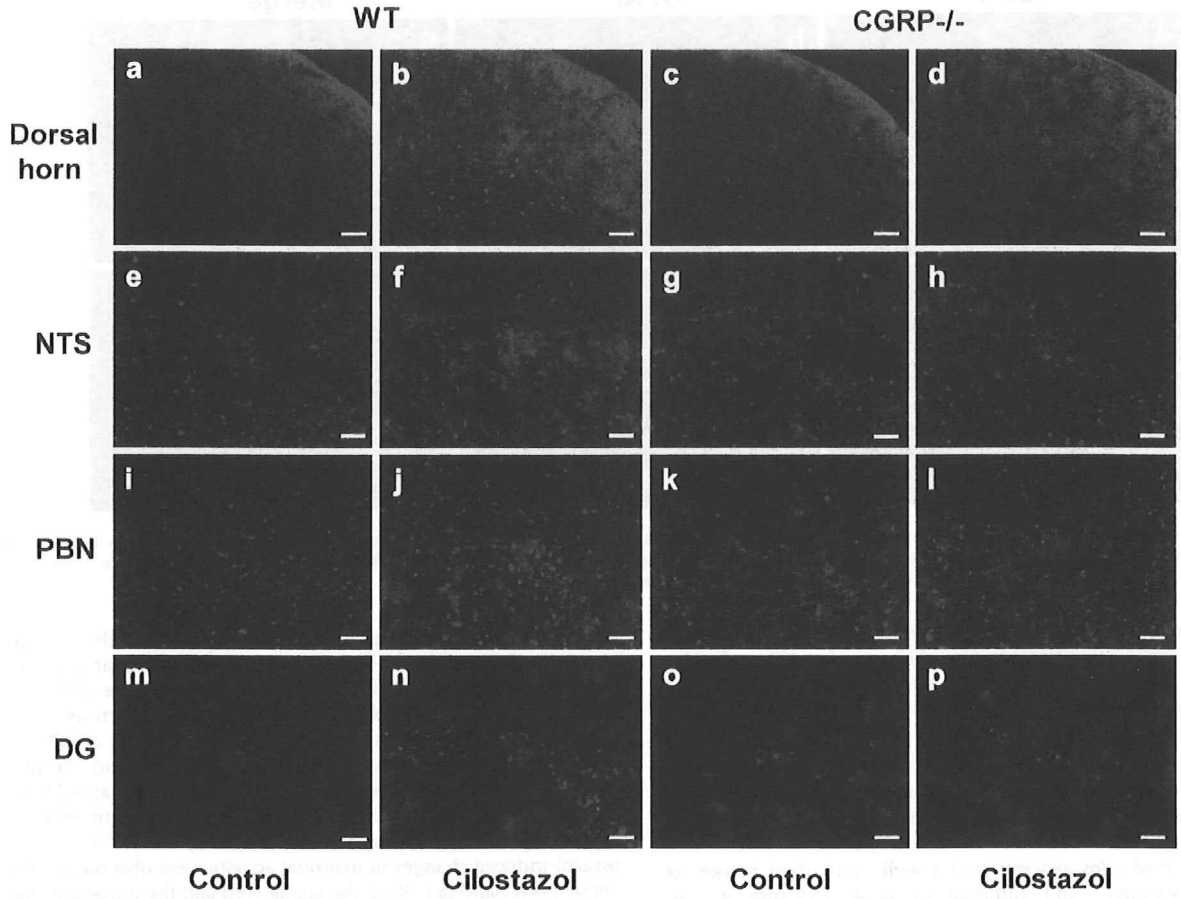

Fig. 6. Effect of cilostazol administration on *c-fos* expression in spinal and supraspinal tissue levels in the WT and CGRP−/− mice. All tissues were removed 4 weeks after oral administration of cilostazol in WT (b, f, g, and n) and CGRP−/− (d, h, l and p) mice, control in WT (a, e, i and m) and CGRP−/− (c, g, k and o) mice. Immunohistochemial expression of *c-fos* in the dorsal horn of the spinal cord (a–d), solitary tract nucleus (e–h), medial parabrachial nucleus (i–l), and dentate gyrus (m–p). Five animals in each group were examined, and typical results are shown. Scale bars = 50 μm.

CGRP−/− mice than in WT mice (Fig. 8). Significant increases in the number of BrdU+/CD31+ ($F_{3,\ 16} = 19.43$, $p < 0.01$) and BrdU+/calbindin-D28k+ ($F_{3,\ 16} = 15.56$, $p < 0.01$) cells but not in that of BrdU+/GFAP + cells was observed in DG after 4-week administration of cilostazol at 160 mg/kg/day in WT mice (Fig. 8). Administration of cilostazol at 30 mg/kg/day also significantly increased the number of BrdU+/CD31 + cells in DG of WT mice ($p < 0.01$) (Fig. 8B). No increase in the number of any of these cells was observed in DG after cilostazol administration in CGRP−/− mice (Fig. 8).

4.7. Effect of cilostazol on the spatial learning in WT and CGRP−/− mice

To determine whether cilostazol improves the cognitive function in mice by increasing IGF-I production in the hippocampus via stimulation of sensory neurons, we examined the effect of cilostazol administration on spatial learning in WT and CGRP−/− mice using the Morris water maze test for 5 consecutive days. Without administration of cilostazol, a significant improvement in spatial learning on days 3, 4, and 5 compared with day 1 was observed in WT mice ($p < 0.01$) (Fig. 9A); no such improvement was noted at any time point during the 5-day study period in CGRP−/− mice (Fig. 9B). In the WT mice, the improvement in spatial learning on days 4 and 5 was significantly enhanced in animals administered cilostazol at 160 mg/kg/day for 4 weeks compared with animals not administered cilostazol (Fig. 9A). Cilostazol did not improve spatial learning at any time during the 5-day study period in CGRP−/− mice (Fig. 9B). Probe tests for reference memory on day 5 revealed a lower percentage of time spent in the trained quadrant by CGRP−/− mice than by WT mice ($F_{1,\ 16} = 80.061$, $p < 0.05$) (Fig. 10). Administration of cilostazol at 160 mg/kg/day resulted in a significantly longer time spent in the trained quadrant than control level in the case of WT ($F_{3,\ 16} = 9.947$, $p < 0.01$) but not CGRP−/− mice (Fig. 10). Swimming speeds in the water maze did not differ between the mice administered cilostazol and the control WT or CGRP−/− mice in any water maze experiments (data not shown).

5. Discussion

In the present study, cilostazol increased CGRP release and cellular cAMP levels in DRG neurons isolated from WT mice *in vitro*. Since PKA activation has been shown to induce sensitization to phosphorylation of TRPV1, and thereby to sensitize sensory neurons to the effects of endogenous agonists (Tominaga et al., 2001), it appeared that cilostazol might increase the release of CGRP from sensory neurons by activating PKA through increase in

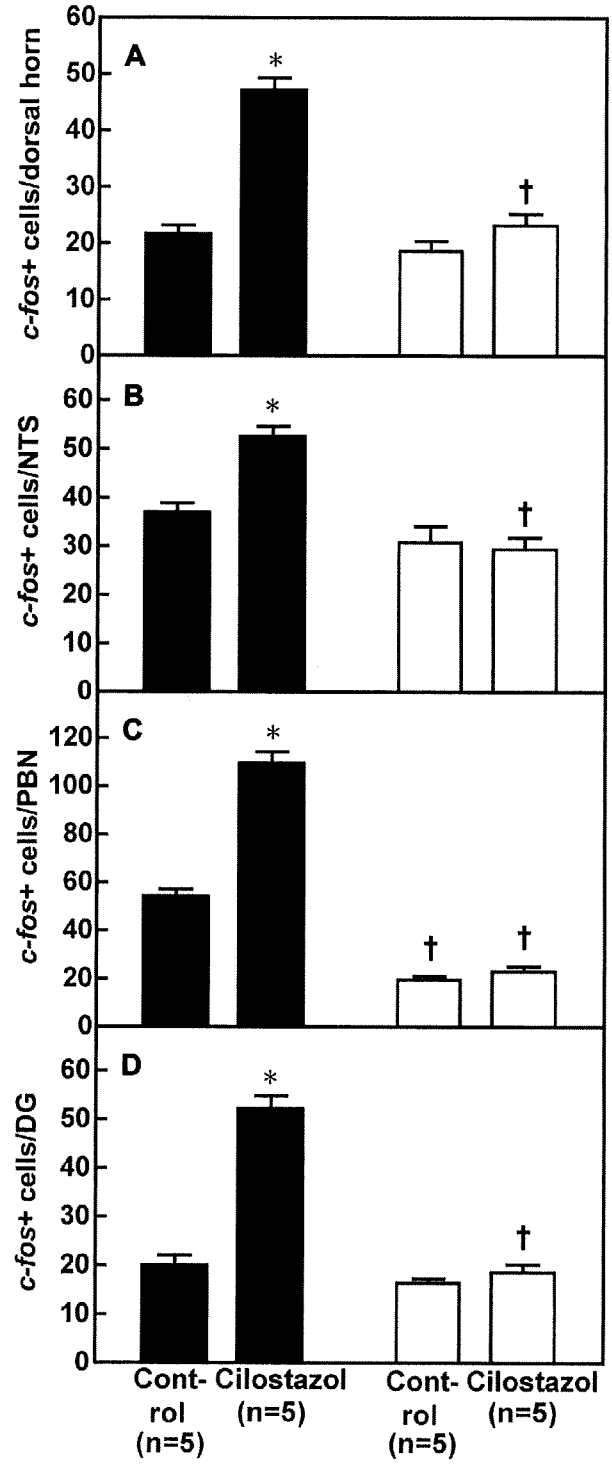

Fig. 7. Effect of cilostazol on the number of *c-fos*-positive cells in the dorsal horn of spinal cord (A), solitary tract nucleus (NTS) (B), medial parabrachial nucleus (PBN) (C), and dentate gyrus (DG) (D) of WT mice and CGRP−/− mice. Data are expressed as means ± S.E.M. from five experiments. Solid bars, WT mice; open bars, CGRP−/− mice. *, $p < 0.01$ vs. control, unpaired student's *t*-test; †, $p < 0.01$ vs. WT mice, two-way ANOVA.

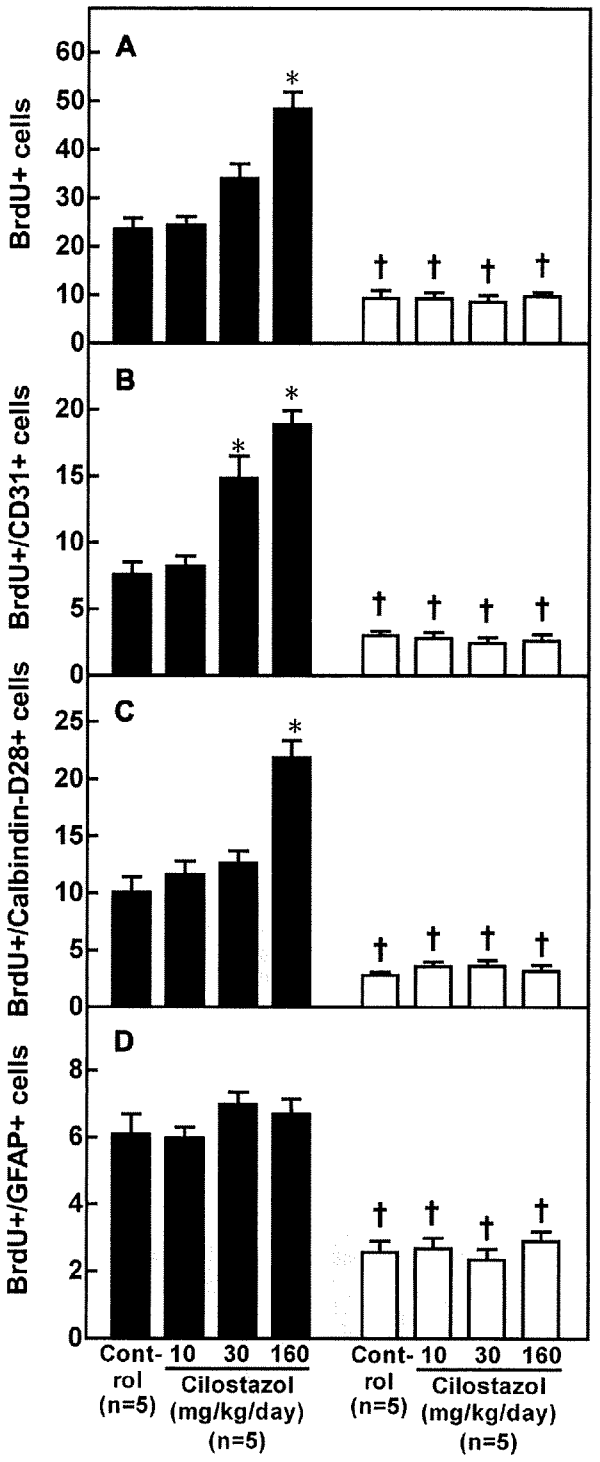

Fig. 8. Quantiative analysis of BrdU-positive cells in WT mice and CGRP−/− mice. All tissues were removed 5 days after BrdU injections. Quantiative analysis of the number of the BrdU+ (A), calbindin-D28k+/BrdU+ (B), CD31+/BrdU+ (C) and GFAP+/BrdU+ (D) cells in DG was performed. Values are expressed as means ± S.E.M. derived from 5 mice in each group. Solid bars, WT mice; open bars, CGRP−/−mice. *, $p < 0.01$ vs. control, one-way ANOVA; †, $p < 0.01$ vs. WT mice, two-way ANOVA.

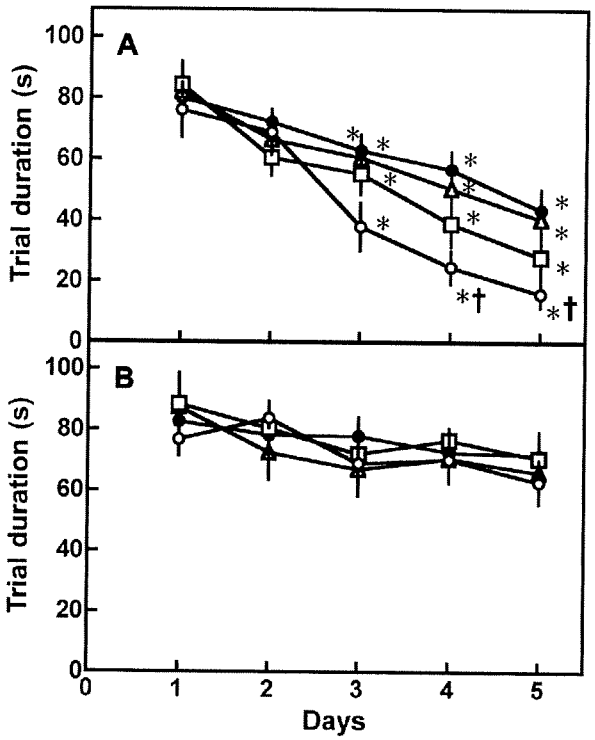

Fig. 9. Effect of cilostazol on spatial learning in WT (A) and CGRP −/− mice (B). Spatial learning was assessed by one trial per day in the Morris water maze for 5 days. Each value is expressed as the mean ± S.E.M. derived from 5 animal experiments. Solid bars, WT mice; open bars, CGRP−/− mice. Closed circles, control; open triangles, cilostazol 10 mg/kg/day; open squares, cilostazol 30 mg/kg/day; open circles, cilostazol 160 mg/kg/day. *, $p < 0.01$ vs. day 1, one-way ANOVA; †, $p < 0.01$ vs. control, two-way ANOVA.

cellular cAMP levels in sensory neurons. Since CGRP increases cAMP levels in DRG neurons (Anderson and Seybold, 2004), whether increase in cAMP levels in DRG neurons treated with cilostazol is due to inhibition of PDE3 or to an effect of CGRP release is unclear at present.

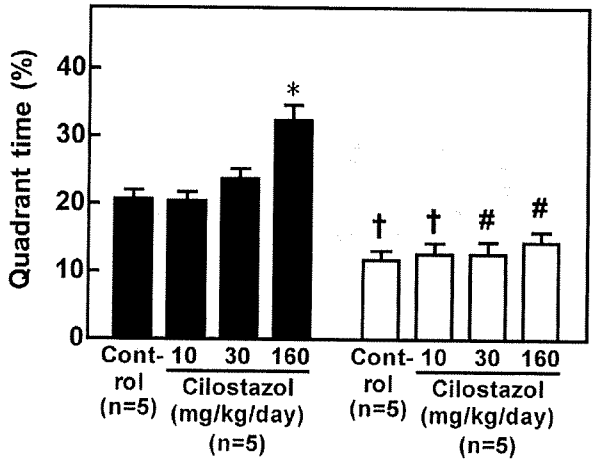

Fig. 10. Effect of cilostazol on the spatial learning function (probe test) in the WT and CGRP −/− mice. Spatial learning was assessed by probe trails in the absence of the platform 2 h after the last trial. Each value is expressed as the mean ± S.E.M. derived from 5 animal experiments. Solid bars, WT mice; open bars, CGRP−/− mice. *, $p < 0.01$ vs. control, one-way ANOVA; †, $p < 0.05$ vs. WT mice, #, $p < 0.01$ vs. WT mice, two-way ANOVA.

Administration of cilostazol (160 mg/kg/day) increased cAMP levels in the DRG and hippocampus in WT mice but not CGRP-knockout mice, suggesting that CGRP might play a critical role in the increase in cAMP levels in these tissues in WT mice administered cilostazol. It thus appears that the increase in cAMP levels in DRG neurons treated with cilostazol *in vitro* and that observed in the DRG of WT mice administered cilostazol *in vivo* cannot be explained by PDE3 inhibition, and is instead due to the release of CGRP from sensory neurons. Furthermore, these observations also suggest that the effects of stimulation of sensory neurons by cilostazol may not be dependent on its inhibition of PDE3, and instead result from undetermined properties of this agent.

Hippocampal tissue levels of IGF-I were significantly lower in CGRP−/− mice and than in WT mice. Oral administration of cilostazol at 160 mg/kg/day increased hippocampal tissue levels of CGRP, IGF-I, and IGF-I mRNA, as well as immunohistochemical expression of IGF-I in WT mice but not CGRP−/− mice. Serum levels of IGF-I were not increased by administration of cilostazol in the present study. These observations strongly suggest that cilostazol promotes the production of IGF-I in the hippocampus by increasing hippocampal CGRP levels. Consistent with this notion, we previously found that stimulation of sensory neurons by capsaicin administration induced transcription and production of IGF-I in various tissues by increasing the CGRP levels (Harada et al., 2007).

IGF-I immunoreactivity was co-localized with immunoreactivity for the astrocyte marker GFAP in the DG of the WT mice administered cilostazol. This observation is consistent with reports that astrocytes can produce IGF-I in the hippocampus (Ye et al., 2004). CGRP has been shown to increase cAMP levels in astrocytes via CGRP receptor activation (Lazar et al., 1991). Because cAMP plays an important role in IGF-I production (Vignery and McCarthy, 1996), stimulation of sensory neurons by cilostazol may increase CGRP levels in the hippocampus, and thereby increase IGF-I production via increase in cAMP levels in astrocytes. Which cells produce CGRP in the hippocampus of the WT mice administered cilostazol is presently unknown.

To examine the mechanism(s) by which afferent sensory information arising from stimulation by cilostazol is transmitted to the hippocampus, we examined levels of *c-fos* expression in spinal and supraspinal nervous tissues in WT mice and CGRP−/− mice after 4-week administration of cilostazol. In WT mice, increase in *c-fos* expression was observed in the dorsal horns (lamina I–II) of the spinal cord and, supraspinally, in the NTS, PBN, and hippocampus after cilostazol administration. These observations strongly suggest that nociceptive information arising from stimulation with cilostazol in the gastrointestinal tract is transmitted via the spino-parabrachial circuits including NTS as a relay point (Castle et al., 2005; Gauriau and Bernard, 2002).

Nonprincipal neurons in the mouse hippocampus have been shown to be immunoreactive for CGRP (Sakurai and Kosaka, 2007). Hippocampal nonprincipal neurons are innervated by GABAergic neurons projecting from the medial septum (Gulyas et al., 1991). Because the medial septum receives sensory input from the PBN where the spinothalamic tracts terminate (Castle et al., 2005), the increase in hippocampal tissue CGRP levels in WT mice administered cilostazol may be a consequence of activation of the hippocampal nonprincipal neurons by GABAergic neurons projecting to them from the medial septum. These observations suggest that CGRP released from hippocampal nonprincipal neurons following cilostazol administration acts on astrocytes via CGRP receptors, and thereby increases IGF-I production in the hippocampus of WT mice.

Because cAMP plays an important role in IGF-I production (Vignery and McCarthy, 1996), the increase in IGF-I levels in hippocampus might be due to direct action of cilostazol on astrocytes. It thus appears likely that cilostazol increases IGF-I

production in the hippocampus via activation of the spino-parabrachial circuits or via an increase of the cAMP levels in astrocytes. However, the latter possibility appears less likely, since hippocampal tissue levels of cAMP were not increased in CGRP−/− mice administered cilostazol.

In contrast to the observations in WT mice administered cilostazol, no *c-fos* induction was observed in spinal or supraspinal nervous tissues of CGRP−/− mice after cilostazol administration. This suggests that cilostazol may stimulate sensory neurons in the gastrointestinal tract, and thereby increase hippocampal IGF-I production, and that CGRP may function as a transmitter in the pathway involved in this sensory nervous relay system. Consistent with this hypothesis, CGRP expression has been reported at synaptic contacts between the primary afferent sensory neurons and the spinothalamic tract neurons in the dorsal horn of the spinal cord (Carlton et al., 1990), in spinothalamic tract cells (Tie-Jun et al., 2001), and in nerve fibers originating from the PBN (Dobolyi et al., 2005).

The proportions of CD31+, calbindin-D28k+, and GFAP + cells among BrdU-immunoreactive cells of the DG in CGRP−/− mice were significantly lower than in WT mice, suggesting that CGRP and/or IGF-I may be closely related to neural stem cell proliferation in the mouse hippocampus. Consistent with this hypothesis, one study has reported that IGF-I is required for angiogenesis in the adult mouse brain (Lopez-Lopez et al., 2004) as well as for neural stem cell proliferation, with effects mediated by epidermal growth factor and fibroblast growth factor-2 (Arsenijevic et al., 2001).

Cilostazol increased the number of BrdU + cells as well as that of BrdU+/calbindin-D28k + cells, but not that of BrdU+/GFAP + cells, in DG of WT mice. Cilostazol had no effect on the numbers of these cells in the DG of CGRP−/− mice. Peripheral infusion of IGF-I has been found to selectively induce angiogenesis via a VEGF-dependent mechanism in the adult mouse brain (Lopez-Lopez et al., 2004) as well as neurogenesis in the adult rat hippocampus (Aberg et al., 2000). These observations strongly suggest that stimulation of sensory neurons by cilostazol may induce angiogenesis and neurogenesis by inducing IGF-I production via increase in CGRP levels in the mouse hippocampus. Since angiogenesis has been shown to provide a favorable environment for neuronal stem cell proliferation via activation of a VEGF-dependent mechanism (Palmer et al., 2000), the hippocampal neurogenesis induced by cilostazol administration in WT mice may be mediated by angiogenesis.

IGF-I exerts beneficial effects against the decline in cognitive function by increasing synaptic plasticity, neurotransmission, and neurogenesis in the hippocampus (Aberg et al., 2000; Fernandez et al., 2007). In the present study, cilostazol significantly improved the spatial learning in WT but not CGRP−/− mice. This suggests that stimulation of sensory neurons with cilostazol may increase the release of CGRP, and thereby induce IGF-I production in the mouse hippocampus, and improve cognitive function. Since it is known that approximately 2–4 weeks are required before newly generated neurons are functionally integrated and begin modifying active hippocampal circuits (Arsenijevic et al., 2001), the cilostazol-induced improvement of cognitive function we observed appeared to be mainly dependent on enhancement of synaptic transmission and plasticity by IGF-I in the hippocampus.

In animals not administered cilostazol, significant improvement of spatial learning on days 3, 4, and 5 compared with that on day 1 was observed in WT mice. In contrast, no such improvement was noted at any time point during the 5-day study period in CGRP−/− mice. These observations strongly suggest that CGRP plays important roles in spatial learning. We previously reported that administration of IGF-I improved spatial learning in CGRP−/− mice (Narimatsu et al., 2009), suggesting that CGRP may play critical roles in spatial learning by increasing IGF-I production.

Cilostazol has been shown to prevent the decline in cognitive function in rats subjected to chronic cerebral hypoperfusion by inhibiting neuronal apoptosis (Lee et al., 2007; Watanabe et al., 2006), suggesting that cilostazol may be useful in preventing cognitive decline in post-stroke patients. Since IGF-I has potent anti-apoptotic activity, as a result of which it reduces the neuronal cell death induced by ischemic insults (Guan, 2008), cilostazol may prevent neuronal cell death by increasing IGF-I production in rats subjected to chronic cerebral hypoperfusion and thereby preventing cognitive decline.

Because the serum levels of IGF-I in patients with Alzheimer's disease are significantly lower than those in controls without dementia (Watanabe et al., 2005), the findings of the present study raise the possibility that stimulation of sensory neurons by cilostazol is useful for improving cognitive function in patients with Alzheimer's disease. Cilostazol may thus be potentially useful for the treatment of cognitive impairment in patients with Alzheimer's disease as well as post-stroke patients.

Taken together, the findings of the present study strongly suggest that peripheral sensory nerve stimulation by cilostazol increases the tissue levels of CGRP in the hippocampus, and thereby induces IGF-I production and improvement of cognitive function in mice.

References

Aberg, M.A., Aberg, N.D., Hedbacker, H., Oscarsson, J., Eriksson, P.S., 2000. Peripheral infusion of IGF-I selectively induces neurogenesis in the adult rat hippocampus. J. Neurosci. 20, 2896–2903.

Anderson, L.E., Seybold, V.S., 2004. Calcitonin gene-related peptide regulates gene transcription in primary afferent neurons. J. Neurochem. 91, 1417–1429.

Arsenijevic, Y., Weiss, S., Schneider, B., Aebischer, P., 2001. Insulin-like growth factor-I is necessary for neural stem cell proliferation and demonstrates distinct actions of epidermal growth factor and fibroblast growth factor-2. J. Neurosci. 21, 7194–7202.

Carlton, S.M., Westlund, K.N., Zhang, D.X., Sorkin, L.S., Willis, W.D., 1990. Calcitonin gene-related peptide containing primary afferent fibers synapse on primate spinothalamic tract cells. Neurosci. Lett. 109, 76–81.

Castle, M., Comoli, E., Loewy, A.D., 2005. Autonomic brainstem nuclei are linked to the hippocampus. Neuroscience 134, 657–669.

Choi, J.M., Shin, H.K., Kim, K.Y., Lee, J.H., Hong, K.W., 2002. Neuroprotective effect of cilostazol against focal cerebral ischemia via antiapoptotic action in rats. J. Pharmacol. Exp. Ther. 300, 787–793.

Daughaday, W.H., Rotwein, P., 1989. Insulin-like growth factors I and II. Peptide, messenger ribonucleic acid and gene structures, serum, and tissue concentrations. Endocr. Rev. 10, 68–91.

Dawson, D.L., Cutler, B.S., Meissner, M.H., Strandness Jr., D.E., 1998. Cilostazol has beneficial effects in treatment of intermittent claudication: results from a multicenter, randomized, prospective, double-blind trial. Circulation 98, 678–686.

Dobolyi, A., Irwin, S., Makara, G., Usdin, T.B., Palkovits, M., 2005. Calcitonin gene-related peptide-containing pathways in the rat forebrain. J. Comp. Neurol. 489, 92–119.

Dray, A., 1995. Inflammatory mediators of pain. Br. J. Anaesth. 75, 125–131.

Eriksson, P.S., Perfilieva, E., Bjork-Eriksson, T., Alborn, A.M., Nordborg, C., Peterson, D.A., Gage, F.H., 1998. Neurogenesis in the adult human hippocampus. Nat. Med. 4, 1313–1317.

Fernandez, S., Fernandez, A.M., Lopez-Lopez, C., Torres-Aleman, I., 2007. Emerging roles of insulin-like growth factor-I in the adult brain. Growth Horm. IGF Res. 17, 89–95.

Gauriau, C., Bernard, J.F., 2002. Pain pathways and parabrachial circuits in the rat. Exp. Physiol 87, 251–258.

Guan, J., 2008. Insulin-like growth factor-1 and its derivatives: potential pharmaceutical application for ischemic brain injury. Recent Pat CNS Drug Discov. 3, 112–127.

Gulyas, A.I., Toth, K., Danos, P., Freund, T.F., 1991. Subpopulations of GABAergic neurons containing parvalbumin, calbindin D28k, and cholecystokinin in the rat hippocampus. J. Comp. Neurol. 312, 371–378.

Harada, N., Okajima, K., Uchiba, M., Kurihara, H., Nakagata, N., 2006. Antithrombin reduces reperfusion-induced liver injury in mice by enhancing sensory neuron activation. Thromb. Haemost. 95, 788–795.

Harada, N., Okajima, K., Kurihara, H., Nakagata, N., 2007. Stimulation of sensory neurons by capsaicin increases tissue levels of IGF-I, thereby reducing reperfusion-induced apoptosis in mice. Neuropharmacology 52, 1303–1311.

Kimura, Y., Tani, T., Kanbe, T., Watanabe, K., 1985. Effect of cilostazol on platelet aggregation and experimental thrombosis. Arzneimittelforschung 35, 1144–1149.

Landi, F., Capoluongo, E., Russo, A., Onder, G., Cesari, M., Lulli, P., Minucci, A., Pahor, M., Zuppi, C., Bernabei, R., 2007. Free insulin-like growth factor-I and

cognitive function in older persons living in community. Growth Horm. IGF Res. 17, 58–66.
Lazar, P., Reddington, M., Streit, W., Raivich, G., Kreutzberg, G.W., 1991. The action of calcitonin gene-related peptide on astrocyte morphology and cyclic AMP accumulation in astrocyte cultures from neonatal rat brain. Neurosci. Lett. 130, 99–102.
Lee, J.H., Park, S.Y., Shin, Y.W., Kim, C.D., Lee, W.S., Hong, K.W., 2007. Concurrent administration of cilostazol with donepezil effectively improves cognitive dysfunction with increased neuroprotection after chronic cerebral hypoperfusion in rats. Brain Res. 1185, 246–255.
Lopez-Lopez, C., LeRoith, D., Torres-Aleman, I., 2004. Insulin-like growth factor I is required for vessel remodeling in the adult brain. Proc. Natl. Acad. Sci. U.S.A. 101, 9833–9838.
Maggi, C.A., Meli, A., 1988. The sensory-efferent function of capsaicin-sensitive sensory neurons. Gen. Pharmacol. 19, 1–43.
Narimatsu, N., Harada, N., Kurihara, H., Nakagata, N., Sobue, K., Okajima, K., 2009. Donepezil improves cognitive function in mice by increasing the production of insulin-like growth factor-I in the hippocampus. J. Pharmacol. Exp. Ther. 330, 2–12.
Oh-hashi, Y., Shindo, T., Kurihara, Y., Imai, T., Wang, Y., Morita, H., Imai, Y., Kayaba, Y., Nishimatsu, H., Suematsu, Y., Hirata, Y., Yazaki, Y., Nagai, R., Kuwaki, T., Kurihara, H., 2001. Elevated sympathetic nervous activity in mice deficient in alphaCGRP. Circ. Res. 89, 983–990.
Palmer, T.D., Willhoite, A.R., Gage, F.H., 2000. Vascular niche for adult hippocampal neurogenesis. J. Comp. Neurol. 425, 479–494.
Ramsey, M.M., Adams, M.M., Ariwodola, O.J., Sonntag, W.E., Weiner, J.L., 2005. Functional characterization of des-IGF-1 action at excitatory synapses in the CA1 region of rat hippocampus. J. Neurophysiol. 94, 247–254.
Rosenfeld, M.G., Emeson, R.B., Yeakley, J.M., Merillat, N., Hedjran, F., Lenz, J., Delsert, C., 1992. Calcitonin gene-related peptide: a neuropeptide generated as a consequence of tissue-specific, developmentally regulated alternative RNA processing events. Ann. N. Y Acad. Sci. 657, 1–17.
Ryan, S.H., Williams, J.K., Thomas, J.D., 2008. Choline supplementation attenuates learning deficits associated with neonatal alcohol exposure in the rat: effects of varying the timing of choline administration. Brain Res. 1237, 91–100.
Sagar, S.M., Sharp, F.R., Curran, T., 1988. Expression of c-fos protein in brain: metabolic mapping at the cellular level. Science 240, 1328–1331.
Sakurai, O., Kosaka, T., 2007. Nonprincipal neurons and CA2 pyramidal cells, but not mossy cells are immunoreactive for calcitonin gene-related peptide in the mouse hippocampus. Brain Res. 1186, 129–143.
Tie-Jun, S.S., Xu, Z., Hokfelt, T., 2001. The expression of calcitonin gene-related peptide in dorsal horn neurons of the mouse lumbar spinal cord. Neuroreport 12, 739–743.
Tominaga, M., Wada, M., Masu, M., 2001. Potentiation of capsaicin receptor activity by metabotropic ATP receptors as a possible mechanism for ATP-evoked pain and hyperalgesia. Proc. Natl. Acad. Sci. U.S.A. 98, 6951–6956.
Trejo, J.L., Llorens-Martin, M.V., Torres-Aleman, I., 2008. The effects of exercise on spatial learning and anxiety-like behavior are mediated by an IGF-I-dependent mechanism related to hippocampal neurogenesis. Mol. Cell Neurosci. 37, 402–411.
van Rossum, D., Hanisch, U.K., Quirion, R., 1997. Neuroanatomical localization, pharmacological characterization and functions of CGRP, related peptides and their receptors. Neurosci. Biobehav. Rev. 21, 649–678.
Vignery, A., McCarthy, T.L., 1996. The neuropeptide calcitonin gene-related peptide stimulates insulin-like growth factor I production by primary fetal rat osteoblasts. Bone 18, 331–335.
Ward, S.M., Bayguinov, J., Won, K.J., Grundy, D., Berthoud, H.R., 2003. Distribution of the vanilloid receptor (VR1) in the gastrointestinal tract. J. Comp. Neurol. 465, 121–135.
Watanabe, T., Miyazaki, A., Katagiri, T., Yamamoto, H., Idei, T., Iguchi, T., 2005. Relationship between serum insulin-like growth factor-1 levels and Alzheimer's disease and vascular dementia. J. Am. Geriatr. Soc. 53, 1748–1753.
Watanabe, T., Zhang, N., Liu, M., Tanaka, R., Mizuno, Y., Urabe, T., 2006. Cilostazol protects against brain white matter damage and cognitive impairment in a rat model of chronic cerebral hypoperfusion. Stroke 37, 1539–1545.
Ye, P., Popken, G.J., Kemper, A., McCarthy, K., Popko, B., D'Ercole, A.J., 2004. Astrocyte-specific overexpression of insulin-like growth factor-I promotes brain overgrowth and glial fibrillary acidic protein expression. J. Neurosci. Res. 78, 472–484.

Contents lists available at ScienceDirect

Diabetes Research and Clinical Practice

journal homepage: www.elsevier.com/locate/diabres

Basic research article

Macrophage foam cell formation is augmented in serum from patients with diabetic angiopathy

Xinglong Cui [a], *Akifumi Kushiyama* [b], *Masayasu Yoneda* [a], *Yusuke Nakatsu* [a], *Ying Guo* [a], *Jun Zhang* [a], *Haruya Ono* [a], *Machi Kanna* [a], *Hideyuki Sakoda* [c], *Hiraku Ono* [d], *Takako Kikuchi* [b], *Midori Fujishiro* [c], *Masashi Shiomi* [e], *Hideaki Kamata* [a], *Hiroki Kurihara* [f], *Masatoshi Kikuchi* [b], *Shoji Kawazu* [b], *Fusanori Nishimura* [g], *Tomoichiro Asano* [a,*]

[a] *Department of Medical Chemistry, Division of Molecular Medical Science, Graduate School of Biomedical Science, Hiroshima University, 1-2-3 Kasumi, Minami-ku, Hiroshima City, Hiroshima, Japan*

[b] *The Institute for Adult Diseases, Asahi Life Foundation, 1-6-1 Marunouchi, Chiyoda-ku, Tokyo, Japan*

[c] *Department of Internal Medicine, Graduate School of Medicine, University of Tokyo, 7-3-1 Hongo, Bunkyo-ku, Tokyo, Japan*

[d] *Department of Medicine, Diabetes Research Center, Albert Einstein College of Medicine, New York, NY, USA*

[e] *Institute for Experimental Animals, Kobe University School of Medicine, Kobe, Hyogo, Japan*

[f] *Physiological Chemistry and Metabolism, Graduate School of Medicine, University of Tokyo, Bunkyo-ku, Tokyo, Japan*

[g] *Department of Dental Science for Health Promotion, Division of Cervico-Gnathostomatology, Graduate School of Biomedical Sciences, Hiroshima University, Japan*

ARTICLE INFO

Article history:
Received 3 April 2009
Received in revised form
18 October 2009
Accepted 22 October 2009
Published on line 24 November 2009

Keywords:
Macrophage
Diabetic angiopathy
Ex vivo assay
Foam cell

ABSTRACT

The differentiation of macrophages into cytokine-secreting foam cells plays a critical role in the development of diabetic angiopathy. J774.1, a murine macrophage cell line, reportedly differentiates into foam cells when incubated with oxidized LDL, ApoE-rich VLDL or WHHLMI (myocardial infarction-prone Watanabe heritable hyperlipidemic) rabbit serum. In this study, serum samples from Type 2 diabetic patients were added to the medium with J774.1 cells and the degree of foam cell induction was quantified by measuring lipid accumulation. These values were calculated relative to the activities of normal and WHHLMI rabbit sera as 0% and 100%, respectively, and termed the MMI (Macrophage Maturation Index). These MMI values reflected intracellular lipids, including cholesteryl ester assayed by GC/MS. Statistical analysis revealed MMI to correlate positively and independently with serum triglycerides, the state of diabetic retinopathy, nephropathy and obesity, but negatively with administration of α-glucosidase inhibitors or thiazolidinediones. Taken together, our results suggest that this novel assay may be applicable to the identification of patients at risk for rapidly progressive angiopathic disorders.

* *Corresponding author.* Tel.: +81 332016781; fax: +81 332016881.
E-mail address: asano-tky@umin.ac.jp (T. Asano).

Abbreviations: BS, blood sugar; sBP, systolic blood pressure; dBP, diastolic blood pressure; TC, total cholesterol; TG, triglyceride; SU, sulfonylurea; α-GI, α-glucosidase inhibitor; BG, Biguanide; TZD, thiazolidinedione; eGFR, estimated glomerular filtration ratio; GC, gas chromatography; AUC, area under the curve.

0168-8227/$ – see front matter
doi:10.1016/j.diabres.2009.10.011

1. Introduction

Macrophages play important roles in the progression of both diabetic microangiopathy [1,2] and macroangiopathy [3–5]. Macrophages invade the dysfunctional vascular endothelium, change into foam cells by taking up lipids, and secrete high levels of several inflammatory hormones, as well as matrix metalloproteases, which contribute to the development of pathological lesions and remodeling. Indeed, foam cells appear even in the early stages of angiopathy, and the accumulation of large numbers of foam cells is often observed in advanced lesions.

Considering that numbers of patients with diabetic angiopathy and metabolic syndrome are rising dramatically worldwide, it is important to develop a method of identifying those with rapidly progressive angiopathic lesions. In this study, we measured patient serum activity inducing the differentiation of J774.1 into foam cells. During foam cell formation from macrophages, numerous factors including oxidized LDL play an enhancing role [6,7], but J774.1 cells reportedly differentiate into foam cells when incubated with oxidized low density lipoprotein (LDL), very low density lipoprotein (VLDL), or myocardial infarction-prone Watanabe heritable hyperlipidemic (WHHLMI) rabbit serum [8]. The WHHLMI rabbit was developed from WHHL rabbits [9], which have a mutated LDL receptor and hypercholesterolemia, such that atherosclerosis develops rapidly [10,11]. The incidence of myocardial infarction in WHHL rabbits was low, while WHHLMI rabbits developed coronary occlusion and spontaneous myocardial infarction reportedly due to having higher amounts of apolipoprotein E-rich VLDL [12–14].

We investigated whether serum activities in diabetic patients inducing the differentiation of J774.1 cells into foam cells, differ according to patient features including metabolic control, development of angiopathic complications, drug treatments, and so on. Our statistical analysis revealed that foam cell-inducing activity correlates positively and independently with serum triglycerides (TG), the state of diabetic retinopathy, nephropathy and obesity, but negatively with administration of α-glucosidase inhibitors (α-GI) or thiazolidinediones (TZD). Such an assay was thus suggested to possibly be applicable to identifying patients at risk for rapidly progressing angiopathic disorders.

2. Materials and methods

2.1. *Reagents and cell culture*

Murine macrophage-like J774.1 cells were purchased from Riken (Tsukuba, Japan), cultured in RPMI 1640 (Sigma) medium supplemented with 10% fetal calf serum (FCS) (Invitrogen), Penicillin 100 U/ml and Streptomycin 100 μg/ml (GIBCO Invitrogen) at 37 °C in 5% CO_2. All reagents were of analytical grade.

Cells were cultured on 96 well plates (IWAKI) for serum stimulation and lipid accumulation assays. At 90% confluence, each well was incubated with serum free RPMI1640 for 24 h, and then stimulated with 2% serum from individual patients for 72 h. The cells were then subjected to lipid accumulation

Table 1 – (a) Coefficients of correlation and their significance for parametric variables and MMI. (b) Means of MMI for all groups classified by non-parametric complications and use of medications. Values are given as means ± SE. (c) Partial regression coefficients and their significances, for variables adjusted for each other but not normalized. Significance is represented by the *p* values at the bottom.

	Coefficients	*p* value
a.		
Age	−0.025	0.827
BS	0.249	0.030*
HbAlc	0.254	0.027*
sBP	0.068	0.562
dBP	0.075	0.518
WBC	0.246	0.032*
AST	0.012	0.917
ALT	0.134	0.248
γGTP	0.146	0.208
TC	−0.077	0.507
HDL	−0.509	2.55×10^{-6}**
TG	0.528	9.68×10^{-7}**
BMI	0.257	0.025*
Cre	0.259	0.024*
eGFR	−0.188	0.104
	−	+
b.		
Gender (M/F)	19.27 ± 4.97	13.33 ± 1.24
Retinopathy	13.18 ± 1.38	26.07 ± 7.54**
Proteinuria	12.05 ± 1.14	25.46 ± 5.91*
IHD	15.35 ± 1.82	11.55 ± 3.09
SU	14.47 ± 2.57	15.69 ± 2.18
α-GI	15.83 ± 2.03	12.12 ± 2.61
TZD	14.80 ± 1.82	17.88 ± 3.10
BG	12.03 ± 1.25	20.85 ± 4.14*
Insulin	13.10 ± 1.57	18.79 ± 3.87
Anti-RA	11.09 ± 1.11	20.54 ± 3.52*
Statin	13.13 ± 1.27	18.73 ± 4.27
Anti-platelet	14.43 ± 0.96	22.22 ± 15.36
	Coefficients	*p* value
c.		
(Intercept)	19.55	0.544
Age	−0.282	0.029*
BS	0.005	0.869
HbAlc	−1.211	0.388
sBP	0.072	0.286
dBP	−0.129	0.231
WBC	0.043	0.560
AST	0.324	0.140
ALT	−0.196	0.179
γGTP	0.005	0.938
TC	−0.086	0.022*
HDL	0.046	0.593
TG	0.088	3.66×10^{-8}**
BMI	0.590	0.099†
Cre	0.496	0.952
eGFR	0.002	0.986
Gender	0.307	0.926
Retinopathy	9.304	0.029*
Proteinuria	9.363	0.017*
IHD	−7.429	0.152
CVD	3.128	0.728
SU	−1.551	0.541
α-GI	−6.307	0.018*

Table 1 (Continued)

	Coefficients	p value
TZD	−8.273	0.158
BG	4.333	0.088†
Insulin	−1.578	0.637
Anti-RA	−0.641	0.802
Statin	0.789	0.748
Anti-platelet	−4.185	0.312

* $p < 0.05$.
** $p < 0.01$.
*** $p < 0.001$.
† $p < 0.1$.

assays using AdipoRed (Cambrex), according to the manufacturer's instructions [15]. In brief, the cells were carefully rinsed with phosphate buffered saline (PBS), and 5 μl of AdipoRed reagent were then added to 200 μl of PBS, followed incubation for 10 min at room temperature. Fluorescence was measured with excitation and emission wavelengths of 485 nm and 572 nm, respectively, by fluorimetry. The value obtained with 2% WHHLMI rabbit serum incubation was taken as the Macrophage Maturation Index (MMI) of 100, while 2% normal rabbit serum incubation yielded an MMI of zero. A calibration curve was obtained by serial dilutions of WHHLMI with normal serum. One raw value was the mean, in relative fluorescence units, of five areas per well, and assays were performed five times to obtain a mean MMI value.

2.2. *Serum sampling*

The subjects were 76 patients (53 males and 23 females), who underwent serum sampling in hospitals affiliated with the Institute for Adult Disease, Asahi Life Foundation. The blood examination data and clinical presentations of patients, obtained in routine clinical practice, were collected at the same time as serum sampling. Stage of diabetic retinopathy was determined within 12 months prior to blood sampling, and stage at the last fundus examination was adopted if several examinations had been performed due to stage instability during the prior 12-month period. Patient characteristics are presented in Table 1. All subjects gave informed consent and the study was verified by the institutional ethics committee.

2.3. *Lipid extraction, purification, and separation by GC/MS*

To analyze lipid profiles of accumulated intracellular lipids in J774.1 cells, total lipids were extracted and purified by the Folch method, as previously described [16]. Then, the lipids were dissolved in *n*-hexane and 1 μl of sample was injected into an RTX-5MS (0.25 mm ID × 30 m, 0.25 μm) column attached to a gas chromatograph (Thermo Finnigan Trace GC 2000) which was connected to a mass spectrometer (Thermo Finnigan Trace MS: scanning range: 1–600 *m/z*). The injection temperature was 250 °C, and oven temperatures were 100 °C (2 min) → (25 °C/min) → 250 °C (20 min) → (10 °C/min) → 270 °C (10 min). Cholesteryl components were detected at 362–368 *m/z* independently of other substances.

2.4. *Statistical analysis*

We quantified non-parametrical data such as type of medication, and the state of diabetic complications into indicator variables. Diabetic neuropathy was not assessed because of its variable clinical presentations, which cannot be quantified adequately for transformation into a simple dummy variable and thus could not be effectively utilized in the relatively small number of subjects in this study. Diabetic retinopathy was initially recorded using the Fukuda Classification [17], and stage A2 or later on the most severely affected side, *i.e.* active and progressive states of retinopathy, were dummied as 1, others as 0. Stage of diabetic nephropathy was omitted because diagnosing nephropathy by estimated glomerular filtration ratio (eGFR) and proteinuria was deemed redundant. The presence of ischemic heart disease (IHD) and/or cardiovascular disease (CVD) was determined based on past events, or past and ongoing therapies for these disorders. All ongoing medical therapy classified in Table 1 was dummied as 1 and others 0, dosage-independently.

Data organizing was achieved with Excel2000 (Microsoft), and hierarchical cluster analysis, described using GENESIS 1.7.2 (IGB-TUG). Other statistical analyses were performed using R 2.6.2 (The R Foundation for Statistical Computing), *i.e.* one-way ANOVA, principal component analysis, multi-regression analysis and logistic regression analysis. The Akaike information criterion (AIC) was used to select the best of a collection of candidate models for this dataset.

3. Results

3.1. *Macrophage Maturation Index*

In the macrophage cell line J774.1, administering WHHLMI rabbit serum (final conc. 2%) time-dependently increased macrophage foaming, and lipid accumulation was observed (Fig. 1a) and quantified (Fig. 1b). WHHLMI rabbits exhibit hypercholesterolemia and hypertriglyceridemia, and develop atherosclerosis spontaneously *in vivo* [9]. Their serum thus has the capacity to induce macrophage foaming *ex vivo*. We termed the relative value of lipid accumulation at 72 h, standardized by serial dilution of serum from a WHHLMI rabbit, the MMI. The intra-assay coefficient of variation (CV) was 5.60% ($n = 8$) and the inter-assay CV was 9.43% ($n = 6$). This bioassay was affected by the status of the J774.1 cell line. Thus, assays must be performed with careful attention to cell viability.

We next investigated the MMI of Type 2 diabetic patients whose characteristics are presented in Table 1, and obtained a value of 15.02 ± 14.76 (Supple. 1).

3.2. *Mining the MMI and other datasets*

To clarify the relationships between MMI and other variables, we obtained sera from patients undergoing routine medical investigations. We organized and applied the data to the following analysis. As shown in Fig. 2a, data from all patients were normalized by variables and aligned in ascending order of MMI values. Herein, a tendency for clinical presentation

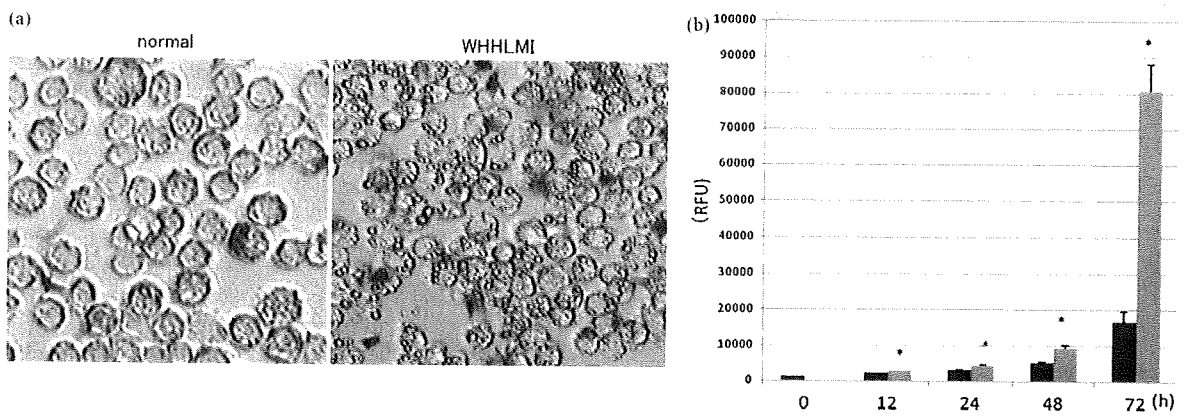

Fig. 1 – (a) Murine macrophage-like cell foaming and lipid accumulation. Cells were cultured on 96-well plates for serum stimulation and lipid accumulation assays. At 90% confluence, each well was incubated with serum free medium for 24 h, and then stimulated with 2% serum from normal and WHHLMI rabbits for 72 h. The cells were then subjected to lipid accumulation assays using Oil red O staining for presentation as an optical microscope image, and using AdipoRed (Cambrex) for quantification. (b) Quantification of lipid accumulation in a time-dependent manner. The cells were carefully rinsed with PBS, and 5 μl of AdipoRed reagent were then added to 200 μl of PBS, followed by incubation for 10 min at room temperature. Fluorescence was measured with excitation and emission wavelengths of 485 nm and 572 nm, respectively, by fluorimetry. One raw value served as the mean of the relative fluorescence, in units, of five areas. The assays were performed five times to obtain a mean MMI value.

with a high MMI to correlate with high Cre, HbA1c, proteinuria and diabetic retinopathy was already apparent, while a low MMI reflected α-GI administration. In Fig. 2b, hierarchical clustering of variables is shown. MMI clustered with TG and renal function. Other variables showed clustering with each other. Only two subjects had CVD, such that power was inadequate for significant variables to be identified by any test. Thus, subjects with CVD were included among those with IHD.

MMI and originally parametric variables are presented in Table 1a. Significant correlations existed between MMI and variables concerning blood glucose control (BS, HbA1c), the inflammatory state (WBC), lipid profile (HDL, TG) and renal function (Cre). When MMI was classified by groups of complications or medications administered, formed retinopathy, proteinuria and administration of BG and anti-RA were associated with significantly higher MMI. Only α-GI administration tended to be associated with lower MMI. With MMI as a criterion variable and others as predictor variables, partial coefficients for regression were calculated, as shown in Table 1c. There was an independent relation between MMI and each variable. Some variables showed inverse correlations or differing significance for the datasets in Table 1a and c, and

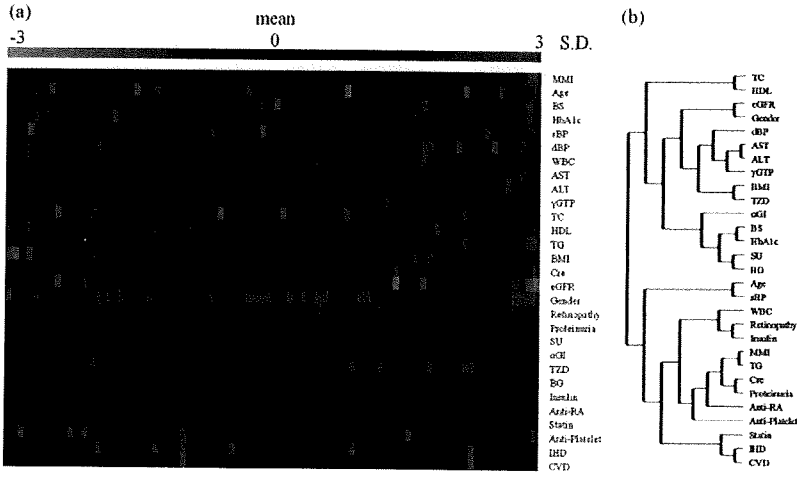

Fig. 2 – (a) Optical presentation of all normalized data from subjects. Parameters were normalized by variables and visualized using GENESIS 1.7.2. Data were aligned in ascending order by MMI from the left for every subject. The tendency was already qualitatively apparent. (b) Hierarchical clustering analysis of variables. Variables presented similar patterns, being clustered in one neighborhood.

Table 2 – Model for multiple regression analysis. Variables were selected by AIC from the variables in Fig. 2. Model: MMI = a × TG (mg/dl) + b × BMI (kg/m^2) + c × (retinopathy) + d × (proteinuria) + e × (α-GI) + f × (TZD) + g.

	Coefficients		Estimated SE	p value
(Intercept)	g	−16.97	5.86	0.0051**
TG	a	0.079	0.0076	8.6×10^{-16}***
BMI	b	0.77	0.24	0.0022**
Retinopathy	c	8.79	2.72	0.0019**
Proteinuria	d	8.28	2.23	0.0004***
α-GI	e	−7.54	2.24	0.0012**
TZD	f	−10.57	3.80	0.0069**

Multiple R^2: 0.75. Adjusted R^2: 0.72.
** $p < 0.01$.
*** $p < 0.001$.

between those in Table 1b and c, probably due to the clinically well-known multi-colinearity (*e.g.* AST and ALT, HDL and TG). In principal component analysis (data not shown), MMI, BS, HbA1c, WBC, HDL, TG, BMI, Cre, retinopathy, proteinuria, BG, Ins, Anti-RA, statin and Anti-Platelet medications were the first principal components.

3.3. *Modeling to account for MMI from routinely obtained parameters*

We subsequently attempted to model a linearly combined collection of variables using stepwise multi-regression analysis. In the model in Table 2, 72% of the variability of MMI was accounted for by variables specified in the model from the adjusted R-squared value. Selection of variables was performed using AIC, that is, the relations of MMI to the variables examined in these models were assumed to be stronger than those of residual variables. Values of TG and BMI, the existence of active retinopathy and/or proteinuria, and administrations of α-GI and TZD were determined and their significance was assessed. Coefficients were not standardized in the model, and thus showed gradients for variables reflecting their own measurement units. For instance, a 1 mg/dl rise in TG proportionally indicated an increase of 0.079, diabetic retinopathy an increase of 8.79, and α-GI administration a reduction of 7.54 in MMI. The fitness of the model is described in Supple. 2 as a QQ plot, basically showing a well-fitted and seemingly appropriate model.

TG was the strongest, possibly even excessively influential, variable. However, if our subjects were limited to those with TG values of no more than 300 mg/dl, the TG effect was no longer selected, and BS, AST, HDL and anti-platelet therapy were newly included in the model. BG administration had a reciprocally worsening effect but it was not significant, and diabetic angiopathies and α-GI were still selected, much as in the model shown in Supple. 3. If the strongest TG effect dissipated, 46.51% was still accounted for by the parameters of the adjusted R^2 value despite the smaller subject number.

3.4. *Prediction of diabetic angiopathy activity by MMI*

Sera from patients with both retinopathy and proteinuria exhibited higher MMI than those from patients with either retinopathy or proteinuria (Fig. 3a). To investigate qualitatively whether MMI predicts diabetic angiopathy, a logistic regression analysis was performed (Fig. 3b), using diabetic angiopathy as the criterion variable, and the risk ratio was then estimated. When MMI rose to +1SD (14.76), the risk ratio (RR) for retinopathy was 1.36 (1.10–1.69, 95% C.I.) and the RR adjusted by all other variables was 1.55 (1.06–2.26). The RR for proteinuria was 1.46 (1.18–1.80), the adjusted RR 1.54 (1.10–2.18).

3.5. *Relationships between cholesteryl ester accumulation and MMI*

Relationships of the MMI values and extracted lipid profiles using GC/MS are presented in Supple. 4a and b. In Supple. 4a, a representative GC chart is shown, and the cholesteryl components detected are shown in Supple. 4b. The sum of the AUCs of cholesteryl ester, other lipids (including FFAs, glycerides analyzed from MS data), and total AUCs tended to correlate positively with MMI (Supple. 5).

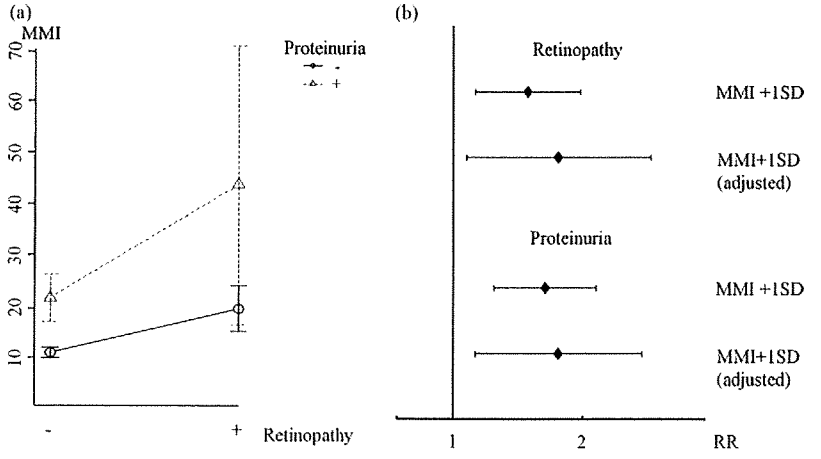

Fig. 3 – (a) Relationships of diabetic angiopathy variables and MMI. Retinopathy and proteinuria together were associated with higher MMI than either retinopathy or proteinuria alone. (b) Risk ratio against increment of MMI (+1SD, 14.76) estimated using logistic regression analysis.